Dynamical modelling of globular clusters: challenges for the robust determination of IMBH candidates

Francisco Aros, Anna Sippel, Alessandra Mastrobuono-Battisti, Abbas Askar, Paolo Bianchini, Glenn Van de ven

Monthly Notices of the ROYAL ASTRONOMICAL SOCIETY

MNRAS **499,** 4646–4665 (2020) doi:10.1093/mnras/staa2821
Advance Access publication 2020 September 19

Dynamical modelling of globular clusters: challenges for the robust determination of IMBH candidates

Francisco I. Aros [1,2,3]★ Anna C. Sippel [3] Alessandra Mastrobuono-Battisti [3,4] Abbas Askar [4] Paolo Bianchini [5] and Glenn van de Ven [1,2]

[1]*Department of Astrophysics, University of Vienna, Türkenschanzstrasse 17, A-1180 Vienna, Austria*
[2]*European Southern Observatory (ESO), Karl-Schwarschild-Str. 2, D-85748 Garching bei München, Germany*
[3]*Max Planck Institute for Astronomy, Königstuhl 17, D-69117 Heidelberg, Germany*
[4]*Lund Observatory, Department of Astronomy and Theoretical Physics, Lund University, Box 43, SE-221 00 Lund, Sweden*
[5]*Observatoire Astronomique de Strasbourg, Université de Strasbourg, CNRS UMR F-7550, Strasbourg, France*

Accepted 2020 September 7. Received 2020 September 7; in original form 2019 December 17

ABSTRACT

The presence or absence of intermediate-mass black holes (IMBHs) at the centre of Milky Way globular clusters (GCs) is still an open question. This is due to either observational restrictions or limitations in the dynamical modelling method; in this work, we explore the latter. Using a sample of high-end Monte Carlo simulations of GCs, with and without a central IMBH, we study the limitations of spherically symmetric Jeans models assuming constant velocity anisotropy and mass-to-light ratio. This dynamical method is one of the most widely used modelling approaches to identify a central IMBH in observations.

With these models, we are able to robustly identify and recover the mass of the central IMBH in our simulation with a high-mass IMBH ($M_{\rm IMBH}/M_{\rm GC} \sim 4$ per cent). Simultaneously, we show that it is challenging to confirm the existence of a low-mass IMBH ($M_{\rm IMBH}/M_{\rm GC} \sim 0.3$ per cent), as both solutions with and without an IMBH are possible within our adopted error bars. For simulations without an IMBH, we do not find any certain false detection of an IMBH. However, we obtain upper limits that still allow for the presence of a central IMBH. We conclude that while our modelling approach is reliable for the high-mass IMBH and does not seem to lead towards a false detection of a central IMBH, it lacks the sensitivity to robustly identify a low-mass IMBH and to definitely rule out the presence of an IMBH when it is not there.

Key words: stars: kinematics and dynamics – globular clusters: general – stars: black holes.

1 INTRODUCTION

With masses between 10^2 M$_\odot$ and 10^5 M$_\odot$, intermediate-mass black holes (IMBHs) are still an elusive population. Ultra-luminous X-ray sources are thought to be accretion signatures of IMBHs, ESO 243-49 HLX-1 being one of the most promising candidates with a minimum mass of 500 M$_\odot$ (Farrell et al. 2009). Recently, the gravitational wave observatories LIGO and Virgo detected an $\sim$ 140 M$_\odot$ black hole (BH) (Abbott et al. 2020a, b). In the local neighbourhood, a few candidates have been suggested through dynamical analysis of nearby globular clusters (GCs) (see e.g. Noyola, Gebhardt & Bergmann 2008; van der Marel & Anderson 2010; Lützgendorf et al. 2013, 2015). Despite their scarce evidence, IMBHs are thought to be the missing link between stellar mass BHs (with masses of $\sim$ 10 M$_\odot$) and supermassive BHs (with masses larger than $\sim 10^5$ M$_\odot$). Furthermore, it has been suggested that IMBHs could be the seeds for supermassive BHs observed at high redshifts in the early universe (see e.g. Haiman 2013, for a review). Possible paths for the formation of IMBHs are the direct collapse of a massive star (Madau & Rees 2001; Spera & Mapelli 2017) and the runaway merger of stars in dense stellar systems (Portegies Zwart et al. 2004), which happens early in the evolution of the stellar system (see also Giersz et al. 2015). A third path may occur later in the evolution of dense stellar systems, where an IMBH can grow from dynamical interactions (Giersz et al. 2015). The latter two scenarios suggest that a dense stellar system, such as GCs, could host a central IMBH.

GCs are bound stellar systems of $\sim 10^5$–10^6 stars, with total masses around 5×10^5M$_\odot$. As their name suggests, most of them have a characteristic spherical shape. GCs are compact stellar systems with half-light radii[1] of the order of a few parsecs. Their compactness and high stellar density make them bright enough to be observed, not only in our galaxy or the Local Group but also beyond (Harris & van den Bergh 1981; Brodie & Strader 2006). Given their relatively high ages, bigger than $\sim$ 10 Gyr, GCs are considered the relics of the formation epoch of galaxies (Vandenberg, Bolte & Stetson 1996; Carretta et al. 2000). The Galactic GCs half-mass relaxation times range from $\sim$ 100 Myr to $\sim$ 10 Gyr (Harris 1996, 2010 edition), making them unique systems for dynamical studies. The short relaxation times allow for mass segregation, i.e. the sorting of higher mass stars towards the cluster centre (Spitzer 1987), while evolving towards a state of partial energy equipartition (see Spitzer 1969; Trenti & van der Marel 2013; Bianchini et al. 2016a).

★ E-mail: francisco.aros@univie.ac.at

[1]Unless mentioned otherwise, we refer to half-light radius as the projected radius containing half of the light in the GC ($R_{\rm h}$), while the half-mass radius is the 3D radius containing half of the mass in the GC ($r_{50\ \rm per\ cent}$).

Different methods have been utilized to find IMBHs in GCs, each relying on two types of signature: accretion of gas by the IMBH or dynamical effects due the presence of the IMBH. On one hand, the accretion signatures in Galactic GCs are dim or non-existent, pointing towards possible IMBHs masses lower than 1000 $M_\odot$ or no IMBHs at all (Tremou et al. 2018). On the other hand (most of), the IMBH candidates in Galactic GCs have been suggested using dynamical signatures. Stars under the direct influence of the central IMBH will follow a Keplerian potential producing a central cusp in the velocity dispersion profile of the GC (Gebhardt, Rich & Ho 2002; Noyola et al. 2008, 2010; van der Marel & Anderson 2010; Lützgendorf et al. 2011, 2012, 2013, 2015; Kamann et al. 2014, 2016, to name a few).

Even with the vast literature analysing the dynamical signatures at the centres of GCs, there is still no consensus regarding the presence or absence of IMBHs in Galactic GCs. The central cusp in velocity dispersion is limited to stars within the radius of influence[2] of the IMBH ($r_{\rm inf}$), which is typically just a fraction of the core radius. Due to the small size of the radius of influence, errors in the determination of the kinematic centre or contamination by bright stars due to crowding in the centre of the GC might hamper the dynamical analysis. Using integral field unit (IFU) spectroscopic data of the central region of NGC 5139 (ω Cen), Noyola et al. (2008) find evidence of an $\sim 40\,000\,M_\odot$ IMBH. For the same cluster, using a sample of proper motion from *HST*, van der Marel & Anderson (2010) find only an upper limit of 18000 $M_\odot$ for the possible IMBH. Both studies have a difference in the position of the kinematic centre, separated by $12''$ (or ~ 0.3 pc at the distance of NGC 5139), which corresponds to 1–2 times the $r_{\rm inf}$, depending on the inferred IMBH mass as given above. However, using another sample of radial velocities, Noyola et al. (2010) show that the detection of the IMBH holds for the different kinematic centres. The discrepancy between both estimates could arise from either the different kind of kinematic data or modelling technique applied. Similarly in the case of NGC 6388, Lützgendorf et al. (2011, 2015) find evidence for an IMBH using velocity maps from integrated spectra, while Lanzoni et al. (2013) do not observe the central velocity dispersion cusp when using the radial velocities of individual stars. More recent observations from IFU with MUSE by Kamann et al. (2018) further support the presence of a central cusp in velocity dispersion. No matter which observational technique is used, the highly crowded centres of GCs add a complex observational challenge.

In addition to the observational limitations due to a small $r_{\rm inf}$, the detection of an IMBH is also made difficult by the limitations in the dynamical models, used to actually identify an IMBH in the observational data. While usually a constant (global) mass-to-light ratio and velocity anisotropy (see Section 2.3) are assumed for the dynamical models, these quantities can vary significantly in a GC. For NGC 5139, van der Marel & Anderson (2010) show how an extended dark mass due stellar remnants is also consistent with the observed velocity dispersion profile. This possibility was also recently explored by Zocchi, Gieles & Hénault-Brunet (2019), who uses a multimass dynamical model, based on distribution functions (DFs), to include a central cluster of stellar-mass BHs, proving that this dark extended population could also produce the central rise in velocity dispersion in NGC 5139. Using a library of *N*-body simulations, Baumgardt et al. (2019) also showed that a cluster of stellar-mass BHs at the centre of NGC 5139 was favoured over a central IMBH, in particular, due to their distinctive effect on the high-velocity stars at the centre of the GC. A similar case was shown by Mann et al. (2019) for 47 Tuc, where a multimass dynamical model with a central cluster of BHs was consistent with the kinematic data, ruling out the necessity for a central IMBH suggested by Kızıltan, Baumgardt & Loeb (2017). This has been confirmed by Hénault-Brunet et al. (2020) with a different type of multimass models.

Simulations of GCs with a central IMBH provide us with a benchmark to study the observational and dynamical modelling limitations that hinder a robust detection of an IMBH via its dynamical signatures. Work in this direction has been done by de Vita et al. (2017). In their work, the authors explore the recovery of IMBH masses in GCs combining Monte Carlo simulations of GCs with a central IMBH (Askar et al. 2017) and mock IFU observations from SISCO (Bianchini et al. 2015), addressing the effects of crowding, contamination due bright stars, and the cluster centre. They find that, even when the actual mass profile is fully known, it is challenging to detect low-mass IMBH or rule out the IMBH solution in cases without a central IMBH. In addition, they show that when the IMBH is detected, the inferred mass is systematically underestimated. They suggest that the reason could be unquantified effects due to energy equipartition and binaries.

In this work, we explore the limitations of dynamical modelling based on Jeans equations to detect a central IMBH and the feasibility of rejecting an IMBH solution when it is truly absent. For this, we will assume rather *perfectly* sampled observational data from realistic simulations of GCs and analyse them with simple, but commonly used, dynamical models. We introduce a set of Monte Carlo simulations in Sections 2.1 and 2.2 and analyse them with Jeans models[3] described in Section 2.3. We focus on the limitations in the dynamical modelling itself, which assumes constant mass-to-light ratio and velocity anisotropy (see Section 2.3), we apply the same modelling pipeline to the simulated GCs in Section 3.1, and then analyse the result of the fittings in Section 3.2. In Section 4, we discuss the reliability of our dynamical models and we conclude with our summary in Section 5.

2 METHODS AND MODEL SETUP

We investigate the kinematic signatures of the presence of an IMBH using Monte Carlo *N*-body models, evolved to 12 Gyr, to analyse and understand the dynamical signatures of the presence of an IMBH, as described in the following sections.

2.1 MOCCA and the Monte Carlo method

The MOCCA-Survey Database I (Askar et al. 2017) is a collection of about 2000 simulated star clusters with different initial conditions that were evolved using the MOCCA code (MOnte Carlo Cluster simulAtor, Hypki & Giersz 2013; Giersz et al. 2013). The MOCCA code is a 'kitchen sink' package that combines treatment of dynamics with prescriptions for stellar/binary evolution and other physical processes that are important in determining the evolution of a realistic star cluster.

Dense star clusters are collisional systems and their evolution is governed by two-body relaxation. In MOCCA, the treatment for relaxation is based on the orbit-averaged Monte Carlo method (Hénon 1971a, b) for following the long-term evolution of spherically

[2]The radius of influence $r_{\rm inf}$ is the distance from the centre of the GC where the cumulative mass of stars (and stellar remnants) is equivalent to the mass of the central IMBH and hence depends crucially on the mass of the IMBH.

[3]Hereafter, we refer as 'models' exclusively to the dynamical models.

Table 1. Initial properties of simulated GCs that were used for our analysis. The first column indicates the simulation name, given by the central object at 12 Gyr, while the second column indicates the symbol used for referring each simulation in all figures. N indicates the initial number of stellar systems, $f_{\rm bin}$ provides the initial binary fraction of the cluster. All these simulations were initially King (1966) models, their central concentration is given by the parameter W_0. $r_{50\%}$ is the initial half-mass radius of the cluster. r_t gives the initial tidal radius. $R_{\rm GC}$ is the Galactocentric radius of the cluster. The final column indicates the prescription for BH natal kick, for 'Fallback' cases, and BH masses and natal kicks are computed using the mass fallback prescriptions of Belczynski, Kalogera & Bulik (2002). For 'No Fallback' cases, BHs are given natal kicks that follow a Maxwellian distribution with $\sigma = 265\,{\rm km\,s^{-1}}$ (Hobbs et al. 2005). The metallicity of all simulations was $Z = 0.001$.

Simulation	Symbol	N	$f_{\rm bin}$ (%)	W_0	$r_{50\%}$ (pc)	r_t (pc)	$R_{\rm GC}$ (kpc)	Central density ($\rm M_\odot\,pc^{-3}$)	BH natal kicks
No IMBH/BHS		1.2×10^6	10	6	2.40	60	3.17	9.8×10^4	No fallback
No IMBH + BHS		1.2×10^6	10	3	1.20	60	3.17	3.1×10^5	Fallback
High-mass IMBH		1.2×10^6	5	9	1.20	60	3.21	3.5×10^7	No fallback
Low-mass IMBH		7.0×10^5	5	9	2.40	60	4.20	2.1×10^6	No fallback
Post core-collapse		1.2×10^6	5	9	7.04	60	3.21	2.3×10^5	No fallback

symmetrical star clusters. This method was subsequently improved by Stodolkiewicz (1982), Stodolkiewicz (1986), Giersz (1998), and Giersz (2001). In this approach, relaxation is treated as a diffusive process and velocity perturbations are computed by considering an encounter between two neighbouring stars. Energy and angular momentum of stars are perturbed at each time-step to mimic the effects of two-body relaxation. The Monte Carlo method combines the particle-based approach of N-body methods with a statistical treatment of relaxation. This allows for inclusion of additional physical processes that are important when simulating the evolution of a realistic star cluster. In MOCCA, stellar and binary evolutions are implemented using the prescriptions provided by the single (SSE) and binary (BSE) codes (Hurley, Pols & Tout 2000; Hurley, Tout & Pols 2002). For computing the outcome of strong dynamical interactions involving binary–single stars and binary–binary stars, MOCCA uses the FEWBODY code (Fregeau et al. 2004), which was developed to carry out small-N scattering experiments, in which case, the time-step for FEWBODY is set to resolve the interaction. Within one MOCCA time-step, many of such interactions can occur and it is also the case for binary systems interacting with an IMBH. MOCCA also includes a realistic treatment for the escape process in tidally limited star clusters as described by Fukushige & Heggie (2000). In this treatment, the escape of an object from the cluster is not instantaneous but delayed, and some potential escapers can get scattered to lower energies and become bound to the cluster again (Baumgardt 2001).

The main advantage of using the Monte Carlo method to simulate the dynamical evolution of a realistic star cluster is speed. MOCCA can compute the evolution of a million-body star cluster within a week. This advantage makes Monte Carlo codes suitable for probing the influence of the initial parameter space on the dynamical evolution of GCs. Given its underlying assumptions, the Monte Carlo method is limited to simulating spherically symmetric clusters with a time-step that is a fraction of the relaxation time. Therefore, it is well suited for following the long-term evolution of a GC but is not ideal for following the evolution on dynamical time-scales. Results from MOCCA have been extensively compared with the results for direct N-body simulations (Giersz, Heggie & Hurley 2008; Giersz et al. 2013; Wang et al. 2016; Madrid et al. 2017). The evolution of global GC parameters and the number of specific objects in MOCCA and direct N-body simulations are in good agreement (Wang et al. 2016; Madrid et al. 2017). These comparisons also serve to calibrate free parameters in the MOCCA code connected with the escape processes and interaction probabilities (Giersz et al. 2013).

2.2 The Monte Carlo simulations

We analyse five simulated GCs with and without IMBHs, taken from the MOCCA-Survey Database I (Askar et al. 2017). Their initial conditions are given in Table 1 and each is named to indicate the type of central object they contain at 12 Gyr (see also Table 2). The *no IMBH/BHS* simulation does not contain an IMBH or a significant number of BHs at 12 Gyr. The *no IMBH + BHS* contains 148 stellar remnant BHs (of the order of $\sim 10\,{\rm M_\odot}$ each) at 12 Gyr. The *high-mass IMBH* cluster hosts a central IMBH of $\sim 13000\,{\rm M_\odot}$ at 12 Gyr, while the *low-mass IMBH* contains an IMBH of $\sim 500\,{\rm M_\odot}$ at 12 Gyr. The simulated cluster labelled *post core-collapse* has reached core-collapse at 12 Gyr and does not contain an IMBH or a significant number of stellar mass BHs.

All these GCs initially followed a King (1966) profile and had 1.2×10^6 stellar systems,[4] except for the *low-mass IMBH*, which initially had 7×10^5 stellar systems. In all cases, a metallicity of $Z = 0.001$ (corresponding to [Fe/H] ~ -1.3) was used for the stars. The initial binary fraction for these simulated GCs is indicated in the third column in Table 1, and their initial binary properties assume a thermal eccentricity distribution, a uniform mass ratio distribution, and a semimajor axis distribution, which is uniform in logarithmic scale [between $2(R_1 + R_2)$ and 100 AU, where R_1 and R_2 are the zero-age main-sequence stellar radii of the binary components]. The simulated GCs had an initial tidal radius of 60 pc and are assumed to have a circular orbit with a velocity of 220 km/s around a point mass-like potential for the galaxy, of which total mass is equal to the enclosed mass inside the Galactocentric radius of each simulated GC (see Table 1).

In all simulated GCs, except the *no IMBH + BHS*, BHs were given the same natal kicks as neutron stars at the moment of formation. The natal kick velocity follows a Maxwellian distribution with $\sigma = 265$ km/s (Hobbs et al. 2005). For the *no IMBH + BHS* cluster, BH masses and natal kicks were modified according to the mass fallback prescription provided by Belczynski et al. (2002). This mass fallback prescription introduces a 'fallback' factor, which gives the fraction of the stellar envelope that falls back on the remnant following its formation. This factor can significantly reduce natal kicks for BHs that have progenitors with zero-age main-sequence masses between 20 and $50\,{\rm M_\odot}$. The reduced natal kicks for BHs

[4] In this context, single and binary systems are understood as 'stellar systems'. The simulated clusters start with 1.2×10^6 single + binary systems, rather than 1.2×10^6 stars.

Table 2. Summary of the properties of the simulated GCs at 12 Gyr. These values were measured directly from the simulations. The first column indicates the simulation name, given by the central object at 12 Gyr, while the second column indicates the symbol used for referring each simulation in all figures. The number of stellar systems (N) includes single and binaries stars. $M_{\rm tot}$ is the total mass of the cluster and $r_{50\%}$ is the half-mass radius, while $L_{\rm tot}$ is the total cluster luminosity and $R_{\rm h}$ is the projected half-light radius. The binary fraction ($f_{\rm bin}$) represents the global fraction including all stellar systems in the simulation. The half-mass mass-to-light ratio ($\Upsilon_{50\%}$) and the half-mass velocity anisotropy ($\beta_{50\%}$) were measured including all stellar systems within the half-mass radius ($r_{50\%}$), while the outer velocity anisotropy ($\beta_{\rm out}$) includes all stars with radii larger than $r_{50\%}$. $M_\bullet$ is the mass of the central IMBH, while $M_{\rm bh}$ is the total mass of stellar BHs within $r_{50\%}$.

Simulation	Symbol	N	$M_{\rm tot}$ ($\times 10^5\,{\rm M}_\odot$)	$r_{50\%}$ (pc)	$L_{\rm tot}$ ($\times 10^5\,L_\odot$)	$R_{\rm h}$ (pc)	$f_{\rm bin}$ (%)	$\Upsilon_{50\%}$ (${\rm M}_\odot/L_\odot$)	$\beta_{50\%}$	$\beta_{\rm out}$	$M_\bullet$ (${\rm M}_\odot$)	$M_{\rm bh}$ (${\rm M}_\odot$)
No IMBH/BHS		1048918	3.56	5.29	1.99	2.50	6.8	1.38	0.03	0.12	0.0	39.98
No IMBH + BHS		971004	3.29	4.99	1.81	2.84	5.7	1.39	0.11	0.37	0.0	1437.61
High-mass IMBH		942585	3.07	5.50	1.81	2.63	2.0	1.26	0.10	0.30	12883.4	0.0
Low-mass IMBH		496159	1.70	6.13	0.95	2.02	3.0	1.40	0.04	0.08	519.3	0.0
Post core-collapse		388631	1.42	5.14	0.83	1.91	3.7	1.24	0.00	−0.03	0.0	15.60

allow the *no IMBH + BHS* cluster to retain about 1300 BHs after 50 Myr of evolution. It had long been thought that BHs that are retained in GCs would efficiently eject themselves through strong dynamical interactions leaving behind at best one or two BHs up to a Hubble time (Kulkarni, Hut & McMillan 1993; Sigurdsson & Hernquist 1993). However, recent theoretical and numerical works have shown that BH depletion might not be so efficient and GCs with moderately long relaxation times that are dynamically young could contain a sizeable number of BHs up to a Hubble time (Breen & Heggie 2013a, b; Morscher et al. 2013; Sippel & Hurley 2013; Heggie & Giersz 2014; Morscher et al. 2015; Wang et al. 2016; Arca Sedda, Askar & Giersz 2018; Askar, Arca Sedda & Giersz 2018b; Weatherford et al. 2018, 2019; Kremer et al. 2019). In the same way, the presence of BHs in GCs has been suggested by the combination of radio and X-ray observations (Maccarone et al. 2007; Strader et al. 2012; Chomiuk et al. 2013; Miller-Jones et al. 2015; Bahramian et al. 2017; Dage et al. 2018; Shishkovsky et al. 2018) and kinematics (Giesers et al. 2018, 2019). These observations suggest the possibility of multiple BHs in GCs. At 12 Gyr, the *no IMBH + BHS* model has lost a significant fraction ($\sim$ 90 per cent) of its retained BHs as the cluster evolves but still retains about 148 of them.

The two simulated clusters that include a central IMBH are called *high-mass IMBH* and *low-mass IMBH*. Both follow the formation scenarios and growth of IMBHs in GCs as seen in MOCCA simulations, which are described in Giersz et al. (2015) and summarized in the following (see also Arca Sedda, Askar & Giersz 2019, for an analysis on all MOCCA simulations that include an IMBH). The *high-mass IMBH* cluster had initially a central density of $3.5 \times 10^7\,{\rm M}_\odot\,{\rm pc}^{-3}$. Typically, for simulations with such high central densities, runaway mergers of main-sequence stars in the first 50 Myr lead to the formation of massive main-sequence stars that can then form an IMBH seed either through a merger or a collision with a stellar mass BH or through direct collapse (see e.g. Portegies Zwart et al. 2004; Spera & Mapelli 2017). This formation scenario occurs early in the evolution of the GC and is described as the 'FAST' scenario in Giersz et al. (2015). On the other hand, in the model *low-mass IMBH* model, the IMBH forms after more than 9 Gyr of cluster evolution via the 'SLOW' scenario described in Giersz et al. (2015). In this scenario, the IMBH forms from the growth of a stellar mass BH by mergers and collisions during the core collapse stage of cluster evolution. The IMBHs formed via the 'SLOW' scenario have masses in the range of 10^2–$10^3\,{\rm M}_\odot$ at 12 Gyr. Both simulations with a central IMBH do not have any stellar BHs within $r_{50\ {\rm per\ cent}}$, because the IMBH efficiently ejects or merges with stellar mass BHs in the cluster (Leigh et al. 2014; Giersz et al. 2015).

The channel of formation also has an impact on the interaction between the IMBH and the surrounding stars. IMBHs formed early on through the 'FAST' scenario produce a more clear central rise in velocity dispersion, while an IMBH formed via the 'SLOW' scenario could lack such clear features at 12 Gyr, as it forms later on during the evolution of the GC (Giersz et al. 2015). In principle, in MOCCA simulations, a low-mass IMBH can wander around the centre of the cluster, which in turn can hamper the formation of the velocity dispersion cusp. As the IMBH mass grows, its movement around the centre decreases, and it should stay fixed for IMBHs with $M_\bullet > 1000\,{\rm M}_\odot$. In MOCCA simulations, IMBHs with $M_\bullet > 1000 \sim 2000\,{\rm M}_\odot$ should produce a clear central rise in the velocity dispersion and surface brightness profiles (Giersz et al. 2015).

At 12 Gyr, the IMBH in the *low-mass IMBH* simulation is almost the innermost object; however, its displacement with respect to the cluster centre is small (2×10^{-4} pc or ~ 10 mas at 5 kpc) and it should not have an effect in the dynamical models. However, as pointed out by de Vita, Trenti & MacLeod (2018), through direct N-body simulations, large displacements of an IMBH with respect the cluster centre will require tailored data-modelling comparisons, and dynamical models under the assumption of spherical symmetry (as the one used in this work and described below in Section 2.3) might introduce a bias on the estimated masses of the IMBH.

The *post core-collapse* simulation starts out as tidally filling, with a half-mass radius of ~ 7 pc. The cluster undergoes stronger mass loss due to tidal stripping, which decreases the number of stars and shortens its relaxation time. Therefore, the cluster is dynamically older and has evolved to a post core-collapse phase at 12 Gyr.

For all the five simulated GCs, we extracted the 12-Gyr MOCCA snapshot, which contains the radial position, radial velocity, tangential velocity, and stellar parameters of each star. The details of how the snapshot was used for our dynamical modelling are provided in subsequent sections. In Table 2, we provide the 12 Gyr properties of each of the five simulated clusters. We have included in this table the total mass of the cluster ($M_{\rm tot}$), its half-mass ($r_{50\ {\rm per\ cent}}$), half-light radii ($R_{\rm h}$), total luminosity ($L_{\rm tot}$), binary fraction ($f_{\rm bin}$), mass-to-light ratio within the half-mass radius ($\Upsilon_{50\ {\rm per\ cent}}$), the inner ($\beta_{50\ {\rm per\ cent}}$) and outer velocity anisotropy ($\beta_{\rm out}$, see equation 3), the mass of the central IMBH ($M_\bullet$), and the total mass in stellar BHs ($M_{\rm bh}$) within the half-mass radius.

2.3 Dynamical modelling

We build dynamical models to characterize the 3D mass profile of the simulated GCs. Our models are built by solving the Jeans equations (Jeans 1922), which allows us to characterize the internal dynamical

state of a stellar system via the velocity moments of its DF $f(\mathbf{x}, \mathbf{v})$. The following description of the Jeans equations is based on chapter 4 of Binney & Tremaine (2008) and section 2 of van der Marel & Anderson (2010).

The dynamical state of a collisionless system is fully determined by the Collisionless Boltzmann Equation:

$$\frac{\partial f}{\partial t} + \sum_{i=1}^{3} \left(v_i \frac{\partial f}{\partial x_i} - \frac{\partial \Phi}{\partial x_i} \frac{\partial f}{\partial v_i} \right) = 0 \,, \tag{1}$$

which represents the conservation of the probability of finding a star within the phase-space of position $\mathbf{x}$ and velocity $\mathbf{v}$, given the DF $f(\mathbf{x}, \mathbf{v})$ and the potential Φ. However, solving and relating equation (1) to observable quantities is not trivial. A simpler approach is to integrate equation (1) over the velocity space assuming that the system is in equilibrium ($\partial f/\partial t = 0$). This provides a set of equations, known as Jeans equations, depending only on the velocity moments, rather than on the more complex DF. The zeroth velocity moment will correspond to the probability of finding a star at a certain position $\nu(\mathbf{x})$. This is not directly observable and it has to be evaluated using either the number density $n(\mathbf{x}) = N_{\rm tot}\nu(\mathbf{x})$ or the luminosity density $j(\mathbf{x}) = L_{\rm tot}\nu(\mathbf{x})$ as proxies (where $N_{\rm tot}$ and $L_{\rm tot}$ are the total number of stars and total luminosity). Here, we use the latter as proxy of the zeroth velocity moment and express all the equations below in terms of $j(\mathbf{x})$ rather than $\nu(\mathbf{x})$. The first velocity moment is the mean velocity $\langle \mathrm{v} \rangle$, while the second velocity moment $\langle \mathrm{v}^2 \rangle = \sigma^2 + \langle \mathrm{v} \rangle^2$ includes the effects of the velocity dispersion σ and the mean velocity $\langle \mathrm{v} \rangle$.

We build spherically symmetric dynamical models by assuming a DF that depends only on the Hamiltonian $H(\mathbf{x}, \mathbf{v})$ and the total angular momentum L. For these models, the first velocity moments are $\langle \mathrm{v}_r \rangle = 0$, $\langle \mathrm{v}_\varphi \rangle = 0$, and $\langle \mathrm{v}_\theta \rangle = 0$, while for the second velocity moments $\langle \mathrm{v}_\varphi^2 \rangle = \langle \mathrm{v}_\theta^2 \rangle$ holds. This allows to define a tangential component as $\langle \mathrm{v}_t^2 \rangle = \langle \mathrm{v}_\theta^2 \rangle + \langle \mathrm{v}_\phi^2 \rangle$ and have an expression for the Jeans equation, which depends only on two unknown variables $\langle \mathrm{v}_r^2 \rangle$ and $\langle \mathrm{v}_t^2 \rangle$:

$$\frac{d}{dr}\left(j(r)\langle \mathrm{v}_r^2 \rangle \right) + j(r) \left(\frac{d\Phi}{dr} + \frac{2\langle \mathrm{v}_r^2 \rangle - \langle \mathrm{v}_t^2 \rangle}{r} \right) = 0 \,. \tag{2}$$

The dependency of the second velocity moments $\langle \mathrm{v}_r^2 \rangle$ and $\langle \mathrm{v}_t^2 \rangle$ is usually described by the velocity anisotropy β as:

$$\beta = 1 - \frac{\langle \mathrm{v}_t^2 \rangle}{2\langle \mathrm{v}_r^2 \rangle} \tag{3}$$

(see Binney & Tremaine 2008), which could take any functional form and allows us to rewrite equation (2) as follows:

$$\frac{d}{dr}\left(j(r)\langle \mathrm{v}_r^2 \rangle \right) + \left(j(r)\langle \mathrm{v}_r^2 \rangle \right) \left(\frac{2\beta}{r} \right) = -\frac{d\Phi}{dr} \,. \tag{4}$$

In our case, we assume a constant velocity anisotropy through the stellar system; under this condition, the second velocity moment $\langle \mathrm{v}_r^2 \rangle$ is:

$$\langle \mathrm{v}_r^2 \rangle(r) = \frac{1}{j(r) r^{2\beta}} \int_r^\infty dr' \, j(r') r'^{(-2\beta)} \frac{\partial \Phi}{\partial r'}(r') \,. \tag{5}$$

The expression for $\langle \mathrm{v}_r^2 \rangle$ is embedded into the coordinate system centred in the stellar system, but as external observers, we usually do not have the full six-dimensional information (i.e. the three position and three velocities). At most, we have available the individual position of each star projected in the sky (x', y'), the line-of-sight velocity ($\mathrm{v_{LOS}}$), the radial ($\mathrm{v_{PMR}}$) proper motion, and the tangential ($\mathrm{v_{PMT}}$) proper motion. These are shown in Fig. 1.

To relate $\langle \mathrm{v}_r^2 \rangle$ with the observations, we integrate it along the line of sight to get a weighted average for the second velocity moments:

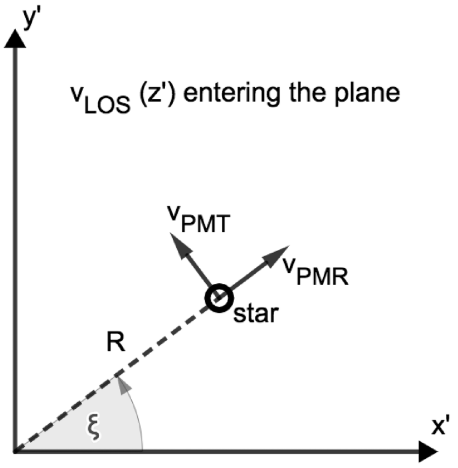

Figure 1. Sky coordinates for the projected velocity components. The star is located at a projected distance R from the cluster centre in the plane of the sky ($x'y'$ plane). The line-of-sight velocity ($\mathrm{v_{LOS}}$) is perpendicular to the plane of the sky, while the radial proper motion ($\mathrm{v_{PMR}}$) follows the direction of the radial vector defined by R, and the tangential proper motion ($\mathrm{v_{PMT}}$) follows the direction of the ξ angle between R and x'.

$$\langle \mathrm{v}_{\rm LOS}^2 \rangle(R) = \frac{1}{I(R)} \int_R^\infty \frac{j(r)dr}{\sqrt{r^2 - R^2}} \left(1 - \beta \left(\frac{r}{R} \right)^2 \right) \langle \mathrm{v}_r^2 \rangle \,, \tag{6}$$

$$\langle \mathrm{v}_{\rm PMR}^2 \rangle(R) = \frac{1}{I(R)} \int_R^\infty \frac{j(r)dr}{\sqrt{r^2 - R^2}} \left(1 - \beta + \beta \left(\frac{r}{R} \right)^2 \right) \langle \mathrm{v}_r^2 \rangle \,, \tag{7}$$

$$\langle \mathrm{v}_{\rm PMT}^2 \rangle(R) = \frac{1}{I(R)} \int_R^\infty \frac{j(r)dr}{\sqrt{r^2 - R^2}} (1 - \beta) \langle \mathrm{v}_r^2 \rangle \,, \tag{8}$$

where $R = \sqrt{x'^2 + y'^2}$ is the radial distance projected in the sky from the centre of the GC to the star and $I(R)$ is the surface brightness of the GC. We model the surface brightness in a similar way (van der Marel & Anderson 2010), using the following function:

$$I(R) = I_0 \times (R/a_0)^{-s_0} \times (1 + (R/a_0)^{\alpha_1})^{-s_1/\alpha_1} \times (1 + (R/a_1)^{\alpha_2})^{-s_2/\alpha_2} \,, \tag{9}$$

where I_0 is a scaling factor, a_0 and a_1 are the inner and outer scale radii, and s_0 gives the slope of a possible central cusp, while s_1, s_2 and α_1, α_2 control the mid and outer slopes. This parametric form allows us to explore a broad range of surface luminosity profiles and easily perform a deprojection to get the luminosity density:

$$j(r) = \frac{-1}{\pi} \int_r^\infty \frac{dR}{\sqrt{R^2 - r^2}} \frac{dI}{dR} \,. \tag{10}$$

To determine the internal mass density profile, we assume a constant mass-to-light ratio Υ_0 and define the stellar mass density profile as $\rho_\star(r) = \Upsilon_0 j(r)$. This simplification is commonly adopted. The total mass of the GC contained within the radius r is then $M(r) = M_\bullet + M_\star(r)$, where $M_\bullet$ is the mass of the possible central BH and $M_\star(r)$ is the stellar mass given by:

$$M_\star(r) = 4\pi \int_0^r \rho_\star(r') r'^2 dr' \,. \tag{11}$$

We express the derivative of the potential Φ as:

$$\frac{d\Phi}{dr} = \frac{GM_\bullet}{r^2} + \frac{GM_\star(r)}{r^2} \,, \tag{12}$$

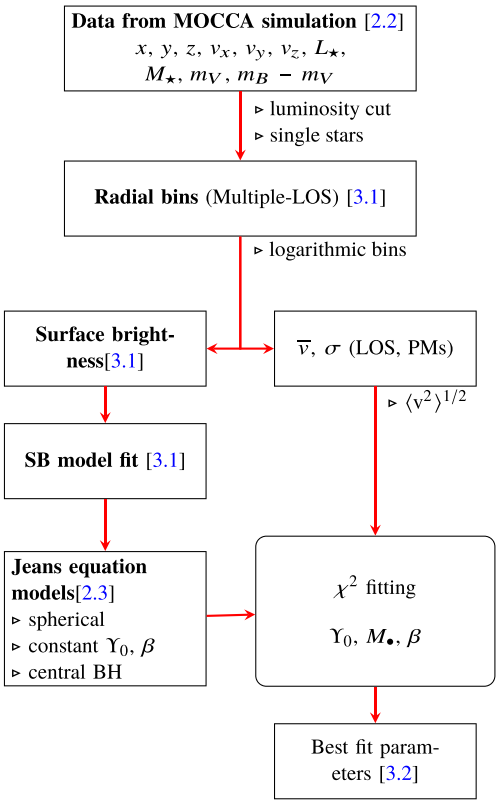

Figure 2. Pipeline for the dynamical analysis of the simulated GCs as described in Section 3.1. We start by extracting the required data from simulated GCs, projected in the sky, from which we generate surface brightness and kinematic radial profiles. The surface brightness profile is used as an input for the dynamical models, which in turn are fitted to the kinematic profiles.

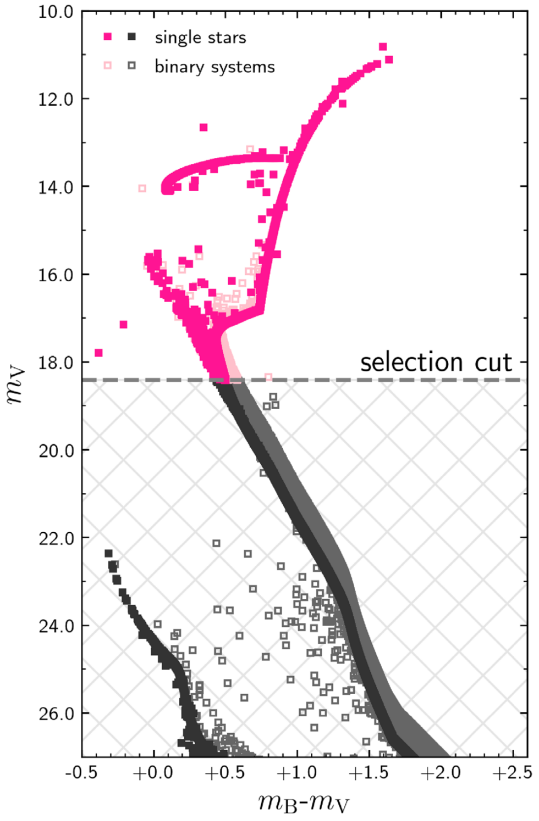

Figure 3. Colour-magnitude diagram for the *no IMBH/BHS* simulation. Single stars are represented by filled symbols, while binary systems are represented by open symbols. We impose a luminosity cut by selecting all stars brighter than one magnitude below the main-sequence turn-off (or an apparent magnitude of $m_V \sim 18.5$ mag at a distance of $D = 5$ kpc, without extinction). This limit is consistent with current observations of line-of-sight velocities and it excludes the most main-sequence stars, the white dwarf sequence, neutron stars, and stellar black holes in the cluster.

where the potential will have a Keplerian component given by the central BH mass ($M_\bullet$) and an extended component given by the mass distribution of stars ($M_\star$).

3 ANALYSIS AND RESULTS

3.1 Pipeline

For all the different data sets mentioned in Section 2.1 and Table 2, we have applied the following blind approach, also summarized in Fig. 2:

(1) For each GC, we select a subsample of stars as our kinematic tracers. The selection, which is the same for each of the GCs, imposes a luminosity cut and the exclusion of all binary systems.

We selected all stars brighter than one magnitude below the main-sequence turn-off as kinematic tracers, which is equivalent to select stars brighter than $m_V = 18.5$ mag at a distance of $D = 5$ kpc (without extinction). As shown in Fig. 3 for the *no IMBH/BHS* simulation, this selection excludes most of the stellar main sequence along with the white dwarf sequence and fainter remnants (neutron stars and stellar BHs). Our magnitude cut resembles the fainter limit adopted by Watkins et al. (2015) for *HST* proper motions of galactic GCs; however, astrometric catalogues can achieve even fainter magnitudes at the central (see Anderson & van der Marel 2010; Libralato et al. 2018, for *HST* proper motions) and outer regions of GCs (Heyl et al. 2017; Bianchini, Ibata & Famaey 2019, for *HST* and *Gaia* proper motions, respectively). On the other hand, while state-of-the-art line-of-sight observations are pushing towards fainter magnitudes, below the main-sequence turn-off (e.g. MUSE Giesers et al. 2019), their observational errors are still large compared to the typical velocity dispersion of GCs. The magnitude cut is agreement with such limitations and allows us to compare line-of-sight velocities and proper motions of our selected kinematic tracers. We have included in Fig. A1, in the appendix, the colour-magnitude diagrams for all five simulated GCs.

Within the selected sample of stellar systems in each simulation, a fraction of them will correspond to binary systems (as shown by the open squares in Fig. 3). Binary stars will have different effects in the measured velocity dispersion depending on the type of kinematic sample. For line-of-sight velocities, the observed radial velocity will be dominated by the orbital velocity of the brightest component rather than their centre of mass velocity; this additional velocity will increase the measured velocity dispersion. Panel (a) of Fig. 4 shows the effect of the binary systems (open squares) in the line-of-sight velocity dispersion compared to a sample that excludes all binaries (filled squares). The individual velocities of each binary component were projected using the COCOA[5] code (Askar et al. 2018a) and then we used the luminosity weighted velocity for each binary system. The bias produced by the orbital velocities of each binary

[5]https://github.com/abs2k12/COCOA

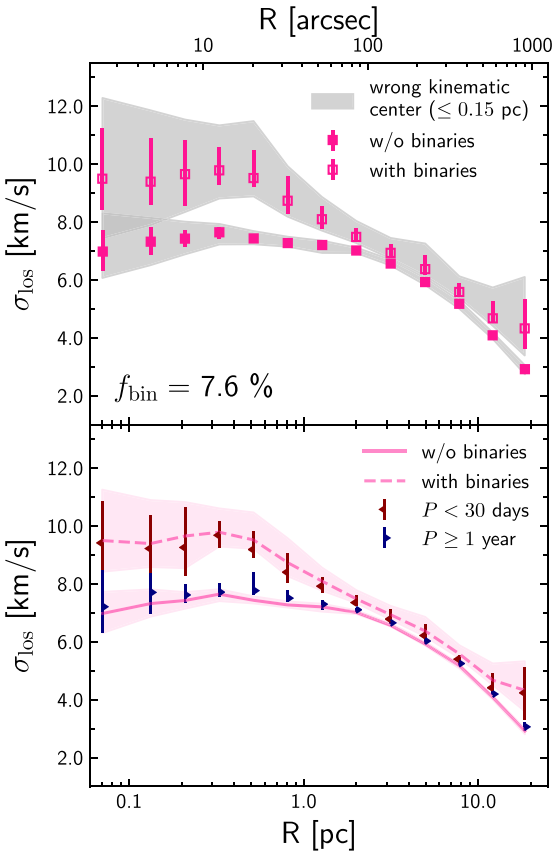

Figure 4. Line-of-sight velocity dispersion for the *no IMBH/BHS* simulation. The simulated GCs have a non-negligible fraction of binary systems, which can increase the observed line-of-sight velocity dispersion, as their measured radial velocity will be dominated by their orbital velocity rather than their centre of mass velocity. The binary systems become harder as their sink towards the centre of the GC. Their intrinsic orbital velocity gets larger and its effect in the observed velocity dispersion becomes more significant. Panel (a) shows the measured velocity dispersion for the selected stellar systems (as in Fig. 3). The sample with binary systems (open squares) has a systematically larger velocity dispersion than the sample, which considers only single stellar systems (solid squares); this difference increases towards the centre where it becomes ~ 2 km/s. The grey shaded areas show the effect on the velocity dispersion caused by an error in the kinematic centre up to R = 0.15 pc (or ~ 6 arcsec at a distance of 5 kpc); this is equivalent to 20 per cent of the core radius of the GC. Not all binary systems have the same influence in the measured velocity dispersion; this is shown in panel (b). Short-period binaries (with $P < 30$ d, left-sided triangles) dominate the increase in velocity dispersion, while binaries with longer periods ($P \geq 1$ yr, right-sided triangles) do not add a significant bias into the velocity dispersion, being similar to the case without binaries. The binary fraction in the selected sample is $f_{\rm bin} = 7.8$ per cent while the fraction of binary stellar system that falls into the short-period binaries is only $f_{\rm bin} = 2$ per cent. The shaded areas in panel (b) represent the error bars for the samples without binaries and with all binaries.

system increases towards the centre of the cluster where binaries become harder.

Panel (b) in Fig. 4 shows the effects in the line-of-sight velocity dispersion for different populations of binary systems, the short-period binaries ($P < 30$ d) dominates the rise in velocity dispersion observed in panel (a), while the long-period binaries ($P \geq 1$ yr), which do not have a large amplitude in their orbital velocity, have a shallower effect. On the other hand, proper motion velocities will not

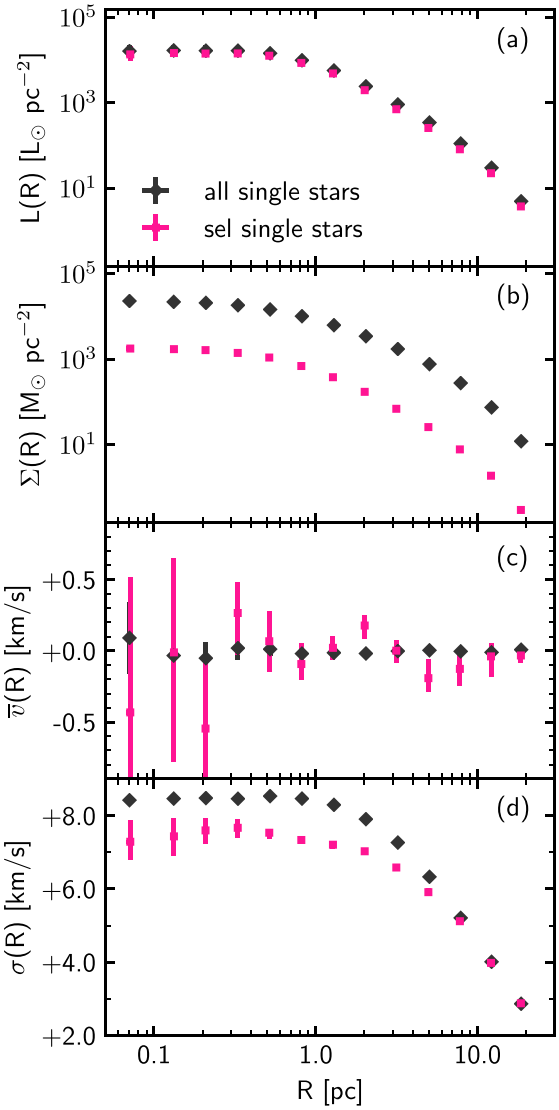

Figure 5. Radial profiles projected in the sky for the *no IMBH/BHS* simulation. In panel (a), we observe no major difference on the luminosity surface density [L(R)] between all the stars and the selected sample; this is expected as the luminosity surface density is dominated by the bright stars. This is not the case for the mass surface density [Σ(R)] in panel (b) where the selection is approximately $\sim$13 times lower than the full sample. Panels (c) and (d) show the line-of-sight mean velocity and velocity dispersion; only in the latter, we observe an $\sim$ 10 per cent difference within 1 $R_{\rm h}$ due energy equipartition effects.

be significantly affected by the orbital motion of the binary system, as the observations will follow the velocity of the centre of mass.

However, as binary systems are more massive than single stars, they will have a systematically lower velocity dispersion than single stars because of partial energy equipartition effects (see Bianchini et al. 2016b, for a discussion). As we expect a larger fraction of binaries towards the centre due to mass segregation, the binary systems will bias the measured velocity dispersion to a lower value (see Fig. A2). This will equally affect line-of-sight velocities and proper motions. Identifying all binaries and excluding them is not usually possible and a few contaminants might remain in real observational samples, even more given our luminosity cut. However, efforts in the direction

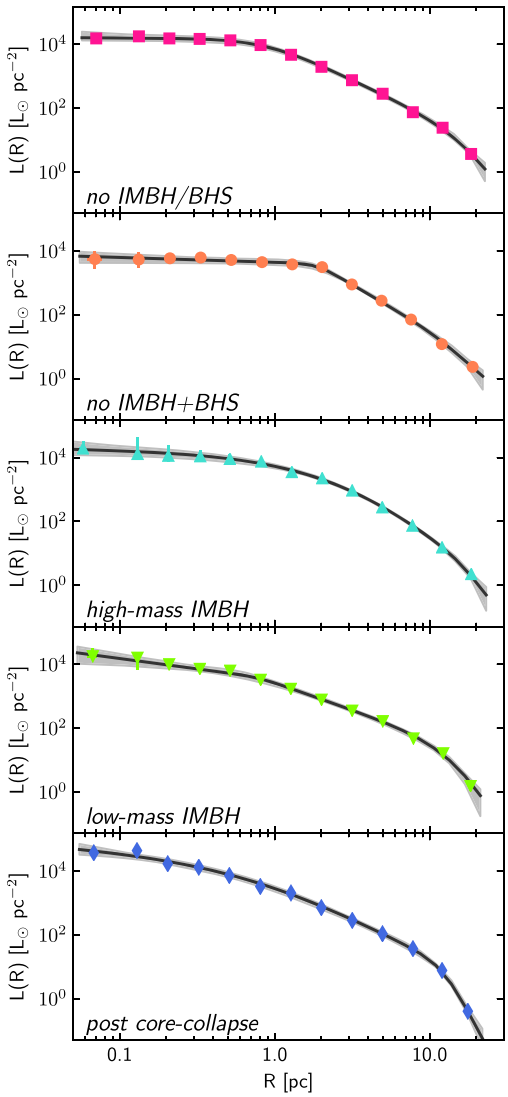

Figure 6. Surface brightness profile and best-fitting model. For each GC, we fit a functional form for the luminosity surface density as given by equation (9). The best fit in each case (black line) will serve as the main ingredient to our dynamical models, as we assume a constant mass-to-light ratio.

to identify binary systems in GCs have been done (see for example Milone et al. 2012; Giesers et al. 2019; Belokurov et al. 2020). The different effects of binaries on the measured velocity dispersion are highly non-trivial and might play against a robust determination of the presence of an IMBH. In this work, we explicitly focus on the limitation introduced by the dynamical modelling in the IMBH mass assessment, and we leave for a follow-up contribution the detailed study of the complex interplay between presence of binaries and observational biases. Furthermore, the sample without binaries is, within errors, still consistent with the sample that includes only long-period binaries, which are more likely to be misidentified with line-of-sight multiepoch observations. For this reason, we have excluded all binary systems from our kinematic sample in the current analysis.

(2) Crowding and the determination of the kinematic centre are two observational effects that have played against the robust determination of IMBHs in GCs (Noyola et al. 2008; van der Marel & Anderson 2010; Lanzoni et al. 2013; Lützgendorf et al. 2013; de Vita et al. 2017). In the case of the former, we assume that we can resolve all stars in the selected sample, while for the centre, we use the same centre for the luminosity and kinematics. The grey shaded area in panel (a) of Fig. 4 shows the effects in the measured velocity dispersion due an error in the kinematic centre determination up to 0.15 pc, approximately 20 per cent of the GC core radius (see de Vita et al. 2017). In comparison, the determination of the centre in NGC 5139 is $\sim$ 10 per cent of its core radius (Noyola et al. 2010).

(3) With the selected sample, we generate radial profiles using the projected data in the (x, y) plane. The profiles follow fixed logarithmic radial bins, which allow us to have information in the central region without requiring an excessive number of bins. Using a fixed binning, and therefore having a varying number of tracers per bin, could potentially lead to low statistics, especially in the central bins. We manage the effect of low statistics by observing the GC from different line of sights. As the simulations have spherical symmetry, this approach allows us to have a distribution of values for each bin without altering the intrinsic radial profiles. We sampled 1000 different line of sights uniformly distributed in a spherical shell and then for each bin, we adopt the median to build the radial profiles and the 16th, and 84th percentiles as an error bar (as the distribution is not necessarily symmetric). Our approach is a simplified version of the projection method described by Mashchenko & Sills (2005), where the probability of each particle to be found in a given bin is calculated as if it were observed from all line of sights.
Fig. 5 shows the luminosity surface density L(R), mass surface density Σ(R), the mean line-of-sight velocity $\bar{v}$(R), and line-of-sight velocity dispersion σ(R) profiles for the *no IMBH/BHS* simulation (pink squares). As a comparison, we also include the profiles when all single stars are considered (black diamonds). No major differences are observed regarding the luminosity surface density, as both samples are dominated by the same bright stars [panel (a) in Fig. 5]. The mass surface density of the selected sample is significantly lower than the full sample of single stars, as our selected sample adds up only to the 4.2 per cent of the total mass of the simulated *no IMBH/BHS* cluster. The velocity dispersion is lower in our selected sample within $R_{\rm h}$, which is an expected effect of energy equipartition (see e.g. Trenti & van der Marel 2013; Bianchini et al. 2016a). It is important to be aware of these differences, as our tracers do not provide the full information about the mass profile of the cluster.

(4) We fit the luminosity surface density profile given by the functional form defined in equation (9). This allows us to cover different types of luminosity surface density profiles and deproject them for the dynamical models. We fit the luminosity surface density with EMCEE (Foreman-Mackey et al. 2013), a Monte Carlo Markov Chain (MCMC) sampler, which allows us to explore the multiparameter space. From the fitting, we save the best-fitting parameters as input for our dynamical models. Fig. 6 shows the luminosity surface brightness profiles and the fit from our MCMC approach for all the different simulations.

(5) We build a grid of dynamic models via the Jeans equations as described in Section 2.3, based on the best-fitting parameters to the surface brightness profile. Each model is defined by three parameters: the mass-to-light ratio (Υ_0), the velocity anisotropy (β), and the mass of the central IMBH ($M_\bullet$). The grid is given by the parameter space: $0.5 \leq \Upsilon_0 \leq 3.5$, $-1.0 \leq \log(M_\bullet/{\rm M}_\odot) \leq 5.0$, and $-1.0 \leq \beta \leq 1.0$. For each model, we calculate the chi square (χ^2_k) as:

$$\chi^2_k = \sum \frac{\left(\langle {\rm v}_k \rangle^{1/2}_{\rm data} - \langle {\rm v}_k \rangle^{1/2}_{\rm model}\right)^2}{\left(\delta \langle {\rm v}_k \rangle^{1/2}_{\rm data}\right)^2}, \quad (13)$$

where k represent each of the observed velocities (LOS, PMR, and PMT). We explore the best-fitting parameters first with only line-of-

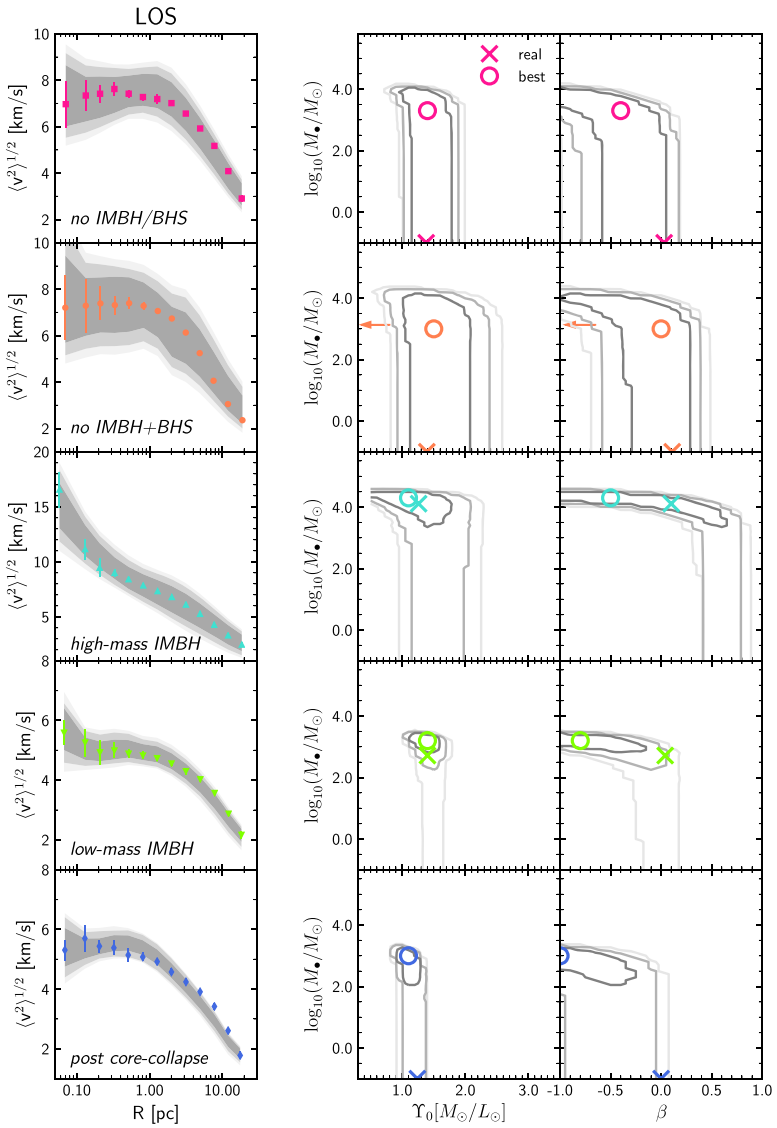

Figure 7. Fitted dynamical models and parameters space when only line-of-sight velocities (LOS) are used for the fit. The left-hand panels show the measured second velocity moment projected in the sky (coloured symbols), while the shaded represent the $\Delta\chi^2 = 3.5$, $\Delta\chi^2 = 7.8$, and $\Delta\chi^2 = 11.3$ regions (from darker to lighter grey). The right-hand panels show the parameter space, whereas the circles mark the best-fitting values (as in Table 3) and the '×' marks the expected value measured directly from the simulations (as in Table 2); the contours represent the $\Delta\chi^2 = 3.5$, $\Delta\chi^2 = 7.8$, and $\Delta\chi^2 = 11.3$ regions. For the *no IMBH + BHS* cluster, we indicate with arrows the total mass in stellar black holes (BHS) within the central 1 pc of the cluster. Overall, the mass-to-light ratio Υ_0 is well constraint by using only LOS velocities. This is not the case for the velocity anisotropy, as the lack of constraints allows the models to have higher masses for the central IMBH at the cost of more tangential orbits. In the case of the *high-mass IMBH*, the cusp in $\langle v^2 \rangle^{1/2}$ is significant enough to detect the IMBH at its centre.

sight velocities, then with only proper motions, and finally with all of them.

3.2 Results

We applied the pipeline described in Section 3.1 to all simulated GCs introduced in Section 2.2 and Tables 1 and 2. Fig. 7 shows our fitted dynamical models when only line-of-sight velocities (LOS) are used, while Fig. 8 shows the case when radial (PMR) and tangential (PMT) proper motions are used together to constrain the best-fitting parameters. Fig. 9, on the other hand, shows the results when LOS velocities and proper motions are used together to constrain the parameters. In each figure, we show the respective second velocity moment profiles ($\langle v^2 \rangle^{1/2}$) used in the χ^2 minimization on the left-sided panels and the parameter space on the right-sided panels. We adopt three relative $\Delta\chi^2$ regions[6] given by $\Delta\chi^2 = 3.5$, $\Delta\chi^2 = 7.8$, and $\Delta\chi^2 = 11.3$ as a guide to our dynamical model and parameter distribution from the χ^2 minimization. We included the best-fitting parameters as an open circle on the right-sided panels, while the

[6]The non-linearity and complexity of our model do not allow us to have a clear value for the degrees of freedom in our χ^2 minimization. The three values adopted here represent the 1σ, 2σ, and 3σ for a χ^2 distribution with 3 degrees of freedom. This is the case for the $\Delta\chi^2$ of a linear model with three free parameters.

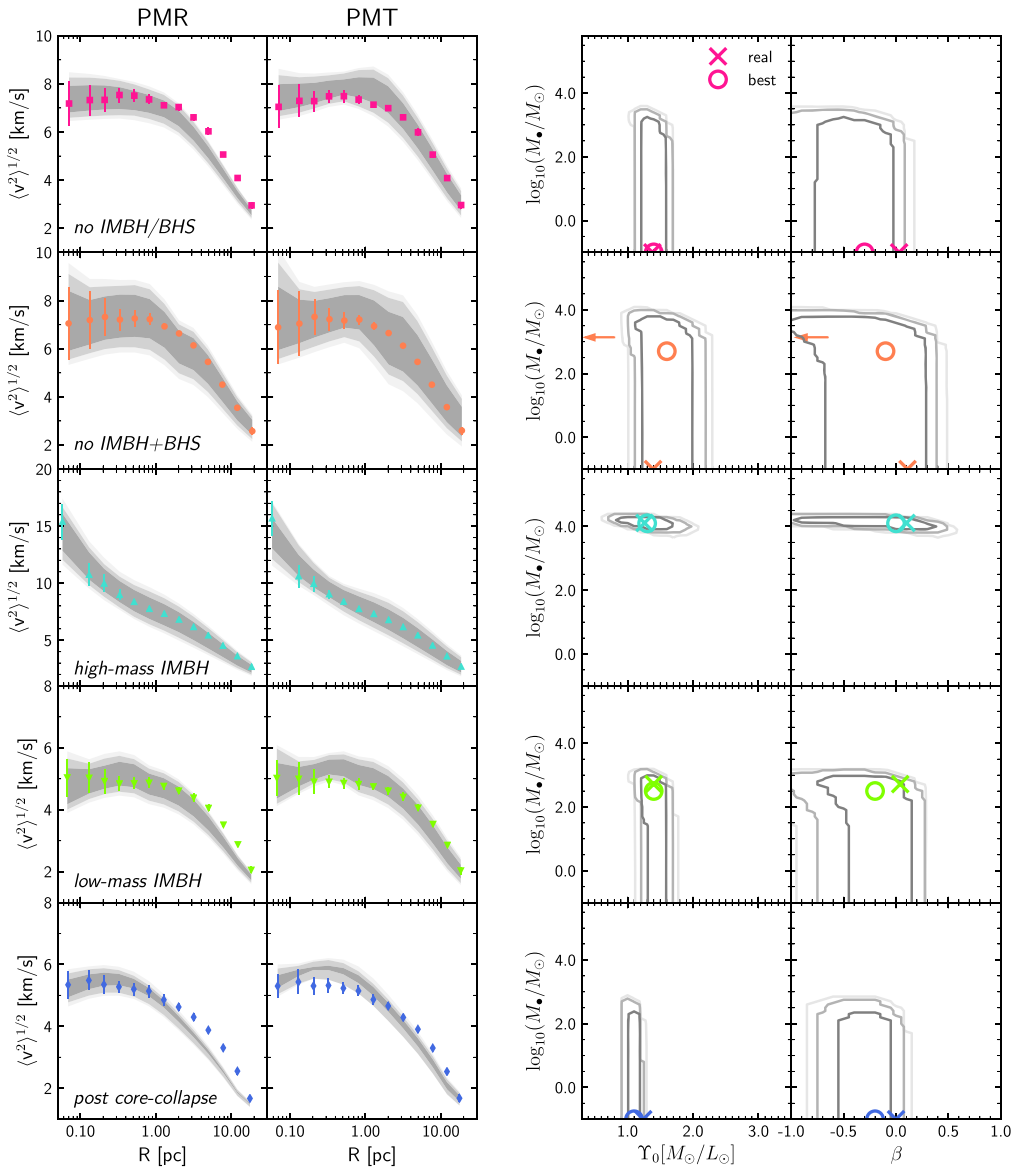

Figure 8. As in Fig. 7, but when only the proper motions (PMR and PMT) are used for the fit. The additional data allow to have a better constraint in the velocity anisotropy, excluding all the models with significant tangential orbits, although the constraints for the mass of the possible central IMBH are similar to when only LOS are used in the fit.

expected values from the simulation are included as an '×' (see Table 2). For the *no IMBH + BHS* simulation, we indicate with an arrow the total mass in stellar BHs within the central parsec of the cluster. Table 3 summarizes the best-fitting parameters for all models and kinematic data; the errors in each parameter are given by the $\Delta\chi^2 = 7.8$ region in the figures (approximately 2σ).

3.2.1 *Constraints from line-of-sight velocities (LOS) only*

Our models can identify the presence of a central IMBH inside the two GCs, which do indeed contain one (see the right-hand side panels of Fig. 7). In the case of the *high-mass IMBH* GC, our best-fitting value is $M_\bullet \sim 2 \pm 2 \times 10^4\,\mathrm{M}_\odot$.[7] While we obtain a detection within the $\Delta\chi^2 = 3.5$ region ($\sim 1\sigma$), which also contains the real value ($M_\bullet = 12883.4\,\mathrm{M}_\odot$), we cannot fully exclude a lower mass IMBH, nor the no IMBH solution with larger confidence levels. This is likely due the lacks of constrains in the velocity anisotropy, as the parameter region with lower mass IMBHs is dominated by highly radial velocity anisotropy ($\beta \gtrsim 0.5$). For the *low-mass IMBH*, we find a detection at $\Delta\chi^2 = 7.8$ level ($\sim 2\sigma$), where the IMBH best-fitting value is $M_\bullet \sim 1.5 \pm 1.4 \times 10^3\,\mathrm{M}_\odot$, around three times the mass of the actual IMBH ($M_\bullet = 519\,M\odot$). This overestimation goes in hand with the high tangential anisotropy of $\beta = -0.8$, inferred from the best-fitting model (see Discussion in Section 4.1 below).

For the *no IMBH/BHS* and *no IMBH + BHS* GCs, we obtain upper limits of $M_\bullet \lesssim 11000\,\mathrm{M}_\odot$ and $M_\bullet \lesssim 17000\,\mathrm{M}_\odot$, respectively. While the whole mass range from the correct solution ($M_\bullet = 0\,\mathrm{M}_\odot$) to the just mentioned upper limits is allowed by the model within

[7]The quoted error bars represent the $\chi^2 \leq 7.8$ confidence region.

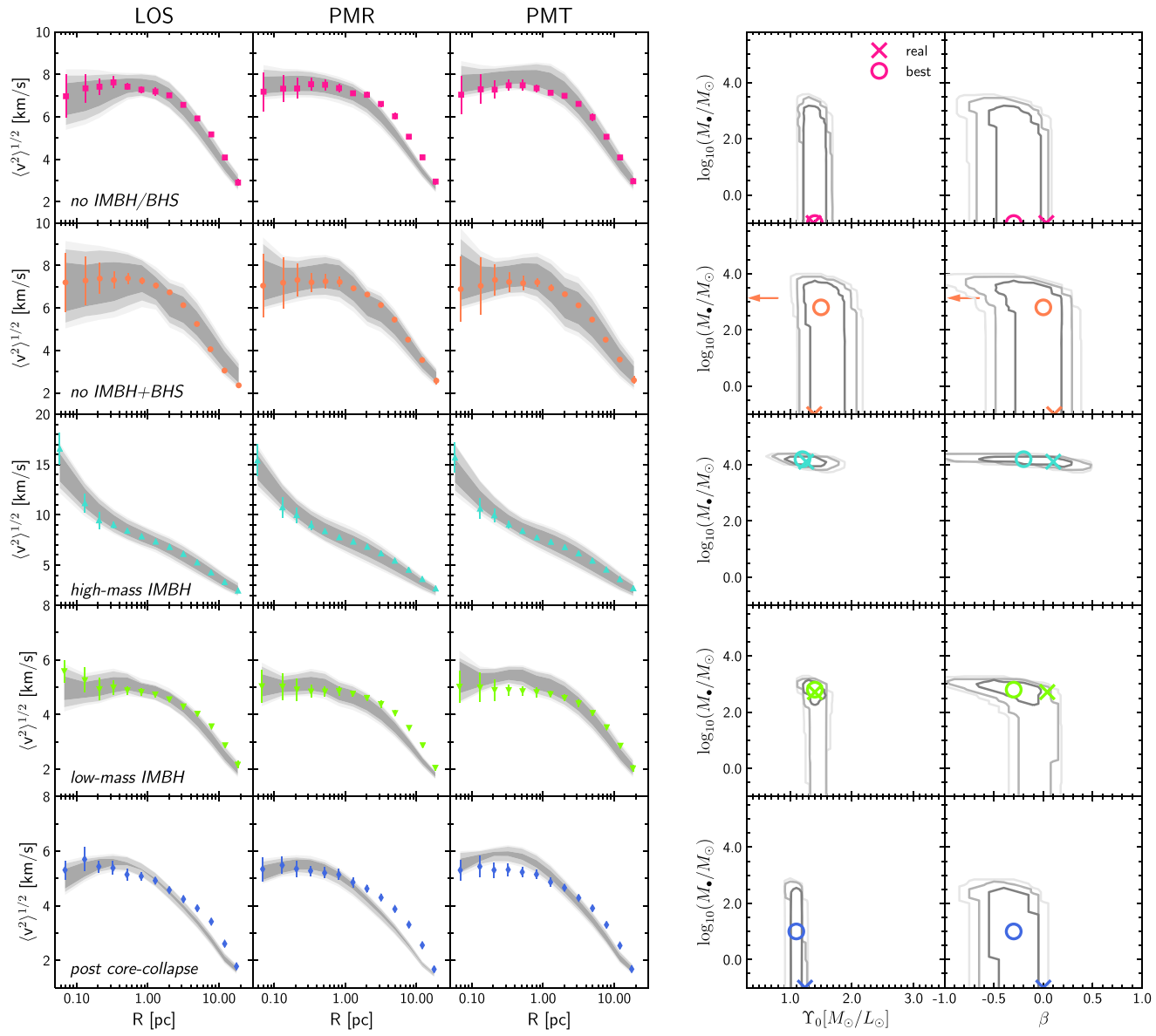

Figure 9. As in Fig. 7, but when all velocities (LOS + PMs) are used for the fit. Compared to the constraints from only the PMs case, the fits do not improve significantly when using the full 3D kinematic data. Now we have a detection for the *low-mass IMBH* within the $\Delta\chi^2 \leq 3.5$ level ($\sim 1\sigma$). However, models without an IMBH are still allowed within the uncertainties ($\Delta\chi^2 \leq 7.8$ level, $\sim 2\sigma$). The upper limits on the inferred mass of the possible IMBH in the cases without one are still in the $M_\bullet \leq 1000\,\mathrm{M}_\odot$ range.

the $\chi^2 \leq 7.8$ confidence region, the best-fitting model indicates a central IMBH of $M_\bullet \sim 2^{+11}_{-2} \times 10^3\,\mathrm{M}_\odot$ for the *no IMBH/BHS* and $M_\bullet = 1^{+17}_{-1} \times 10^3\,\mathrm{M}_\odot$ for the *no IMBH + BHS*. Finally, although the *post core-collapse* GC does not have a central IMBH, the best-fitting model suggests a central IMBH of $M_\bullet = 1^{+1.5}_{-1} \times 10^3\,\mathrm{M}_\odot$, which is detected within 1σ. In a similar fashion than for the *low-mass IMBH*, the inferred mass of the IMBH is bound to a tangential anisotropy ($\beta = -1.0$, at the edge of our parameter space).

As expected, we cannot constrain the velocity anisotropy with only LOS velocities. Fig. 7 shows the existence of a correlation between the mass of the possible IMBH and the velocity anisotropy for each of the five analysed GCs. Dynamical models with a significant tangential anisotropy allow for a larger central IMBH mass (commonly referred to as mass-anisotropy degeneracy, see Section 4.1). Note that for all GCs, the correlation becomes stronger for dynamical models with central IMBH masses higher than $1000\,\mathrm{M}_\odot$. In all simulated GCs, we observe that our models are consistent with the observed kinematics. For the case of the *no IMBH + BHS* simulation, we notice that our models overestimate the second velocity moment at $R \gtrsim 2R_\mathrm{h}$ (or $R \gtrsim 6\,\mathrm{pc}$).

3.2.2 *Constraints from proper motions (PMs) only*

The second velocity moments for the proper motions have a different parametric dependency with the velocity anisotropy (see equations 7 and 8), adding an additional constraint. This improves the constraints for our models when compared with the case with only line-of-sight velocities, as the degeneracy between the velocity anisotropy and the

Table 3. Best-fitting parameters for all the simulated GCs and velocity data used for the fits. The error bars represent the region defined by $\Delta\chi^2 \leq 7.8$ (approximately 2σ, see footnote 6). The first row for each GC indicates the expected values as indicated in Table 2.

Model	Data	Υ_0	$\log(M_\bullet/\mathrm{M}_\odot)$	β
No IMBH/BHS		1.38	–	0.03
	LOS	$1.4^{+0.45}_{-0.55}$	$3.3^{+0.75}_{-4.35}$	$-0.4^{+0.55}_{-0.65}$
	PMs	$1.4^{+0.25}_{-0.25}$	$-1.0^{+4.45}_{-0.05}$	$-0.3^{+0.35}_{-0.75}$
	ALL	$1.4^{+0.25}_{-0.25}$	$-1.0^{+4.45}_{-0.05}$	$-0.3^{+0.35}_{-0.45}$
No IMBH + BHS		1.39	–	0.11
	LOS	$1.5^{+0.85}_{-0.75}$	$3.0^{+1.25}_{-4.05}$	$-0.0^{+0.35}_{-1.05}$
	PMs	$1.6^{+0.55}_{-0.55}$	$2.7^{+1.25}_{-3.75}$	$-0.1^{+0.45}_{-0.95}$
	ALL	$1.5^{+0.55}_{-0.35}$	$2.8^{+1.05}_{-3.85}$	$-0.0^{+0.25}_{-0.75}$
High-mass IMBH		1.26	4.11	0.10
	LOS	$1.1^{+0.95}_{-0.65}$	$4.3^{+0.25}_{-5.35}$	$-0.5^{+1.25}_{-0.55}$
	PMs	$1.3^{+0.65}_{-0.55}$	$4.1^{+0.25}_{-0.25}$	$-0.0^{+0.45}_{-1.05}$
	ALL	$1.2^{+0.55}_{-0.45}$	$4.2^{+0.15}_{-0.35}$	$-0.2^{+0.65}_{-0.85}$
Low-mass IMBH		1.40	2.72	0.04
	LOS	$1.4^{+0.25}_{-0.35}$	$3.2^{+0.25}_{-0.95}$	$-0.8^{+0.85}_{-0.25}$
	PMs	$1.4^{+0.25}_{-0.25}$	$2.5^{+0.65}_{-3.55}$	$-0.2^{+0.45}_{-0.85}$
	ALL	$1.4^{+0.15}_{-0.25}$	$2.8^{+0.35}_{-3.85}$	$-0.3^{+0.45}_{-0.65}$
Post core-collapse		1.24	–	0.0
	LOS	$1.1^{+0.25}_{-0.25}$	$3.0^{+0.35}_{-4.05}$	$-1.0^{+0.95}_{-0.05}$
	PMs	$1.1^{+0.15}_{-0.15}$	$-1.0^{+3.75}_{-0.05}$	$-0.2^{+0.25}_{-0.55}$
	ALL	$1.1^{+0.15}_{-0.15}$	$1.0^{+1.75}_{-2.05}$	$-0.3^{+0.25}_{-0.45}$

mass of the central IMBH is reduced. Our models, however, show some limitations as when using proper motions, they become less consistent with the observed kinematics. For the *no IMBH/BHS*, *low-mass IMBH* and *post core-collapse* GCs, the models fail to mutually fit the radial (PMR) and tangential (PMT) proper motions.

With the additional constraints provided by proper motions, we find a clear 3-σ detection for the *high-mass IMBH* GC and a best-fitting value of $M_\bullet \sim 1.2^{+1.2}_{-0.6} \times 10^4\,\mathrm{M}_\odot$, which is consistent with the real mass of the central IMBH.

The best fit for the *low-mass IMBH* reduces to $M_\bullet \sim 0.3^{+1.2}_{-0.3} \times 10^3\,\mathrm{M}_\odot$, which slightly underestimates the mass of the central IMBH. While we recover a best-fitting value that is more consistent with the real IMBH mass, we do not find a clear detection at 1σ, nor at 2σ; the 2-σ errors allow for a range of masses of $(0\,\mathrm{M}_\odot, 1584\,\mathrm{M}_\odot)$ for the central IMBH.

The constrains for the *no IMBH/BHS* and *no IMBH + BHS* GCs also improve. The upper limits reduce to $M_\bullet \lesssim 3100\,\mathrm{M}_\odot$ and $M_\bullet \lesssim 9900\,\mathrm{M}_\odot$, respectively. The best-fitting value for the *no IMBH/BHS* is $M_\bullet \sim 0^{+3.1} \times 10^3\,\mathrm{M}_\odot$, which is consistent with no central IMBH. For the *no IMBH + BHS* GC simulation, the best fit is now $M_\bullet \sim 0.5^{+9.4}_{-0.5} \times 10^3\,\mathrm{M}_\odot$, more consistent with the no IMBH solution. However, within 2σ, it is not possible to fully rule out a higher mass IMBH.

The *post core-collapse* GC also shows an improvement with a best-fitting IMBH mass, which is consistent with zero ($M_\bullet \sim 0.0^{+0.6} \times 10^3\,\mathrm{M}_\odot$). The upper limit reduces to $M_\bullet \lesssim 630\,\mathrm{M}_\odot$, given the additional constraints on the velocity anisotropy with a recovered value of $\beta = -0.2^{+0.25}_{-0.55}$, which is closer to the actual value obtained from the simulation ($\beta_{50\ \mathrm{per\ cent}} = 0.0$).

3.2.3 *Constraints from the full kinematic sample (LOS + PMs)*

When the full kinematic sample is used to constrain the parameter space, as shown in Fig. 9, we observe similar constraints on the different $\Delta\chi^2$ confidence regions as in the only proper motions case. The IMBH in the *high-mass IMBH* GC is again clearly identified with an inferred mass of $M_\bullet \sim 1.5 \pm 0.9 \times 10^4\,\mathrm{M}_\odot$, while for the central IMBH in the *low-mass IMBH* simulation, we find $M_\bullet \sim 0.6^{+0.9}_{-0.6} \times 10^3\,\mathrm{M}_\odot$ and its presence is recovered within 1-σ level. However, for larger confidence regions, we have models that still are consistent with a lower mass or no IMBH solution.

As in the case with only proper motions, the best-fitting value for the *no IMBH/BHS* GC is consistent with not having an IMBH ($M_\bullet \sim 0^{+3.2} \times 10^3\,\mathrm{M}_\odot$), while still allowing a large upper limit ($M_\bullet \lesssim 2800\,\mathrm{M}_\odot$). Similarly, for the *no IMBH + BHS* GC, we obtain an upper limit of $M_\bullet \lesssim 7900\,\mathrm{M}_\odot$, which has improved from the only proper motion case. The best-fitting value is now $M_\bullet \sim 0.6^{+7.3}_{-0.6} \times 10^3\,\mathrm{M}_\odot$, the range of masses covered by the 2-σ level goes from $0\,\mathrm{M}_\odot$ to $7900\,\mathrm{M}_\odot$. Also for the *post core-collapse* GC, we find a similar result as when only proper motions are used with an upper limit of $M_\bullet \sim 630\,\mathrm{M}_\odot$, while the best-fitting value of $M_\bullet = 10^{+620}_{-10}\,\mathrm{M}_\odot$ is consistent with not having an IMBH.

For all clusters, the global mass-to-light ratio (Υ_0) is well constrained, while the velocity anisotropy (β) shows a significant improvement for all clusters with the exception of the high-mass IMBH, once the proper motions are considered (see Fig. A3). In the case of the *high-mass IMBH*, the velocity anisotropy does not show the same level of improvement after including the proper motions, as the Keplerian rise in velocity dispersion dominates over the velocity anisotropy in the inner kinematics. However, their inclusion allows the exclusion of highly radial anisotropic models.

As in the case when only proper motions are considered, we notice that our models are not fully consistent with the kinematic data; this is particularly true for the *post core-collapse* GC. These discrepancies are originating in the assumptions of our models and show the limitations they bring into the fitting. In the following section, we discuss further how the assumptions of constant velocity anisotropy and mass-to-light ratio affect the modelling and the detection of a possible IMBH.

3.2.4 *Additional kinematic samples*

To explore the effects of our selection criteria (as described in Section 3.1), we applied the dynamical models to three additional kinematic samples. Fig. A5, in the appendix, shows the constraints in the parameter space for the mass-to-light ratio and mass of the possible central IMBH for two fainter magnitude cuts: 4.6 mag below the main-sequence turn-off, following current lower limits for precise proper motions at the cluster centre (Anderson & van der Marel 2010; Libralato et al. 2018), and 7.5 mag below the main-sequence turn-off (Heyl et al. 2017), which is still possible only for proper motions outside the cluster's R_h, but works as an extreme hypothetical case. We do not observe any significant difference with our results for the brightest selection. We notice, though, that for the fainter magnitude cuts, the best-fit value for Υ_0 increases; this is expected due to the larger fraction of low-mass stars that have a systematically larger velocity dispersion (as in Fig. 5). The third case we explored includes long-period binaries ($P > 1$ yr) as in panel (b) of Fig. 4. The comparison with our main results is illustrated in Fig. A6 and we, once again, do not observe any significant difference between our main results and the sample including long-period binaries, which is also expected as both kinematic samples are similar (see Fig. A2).

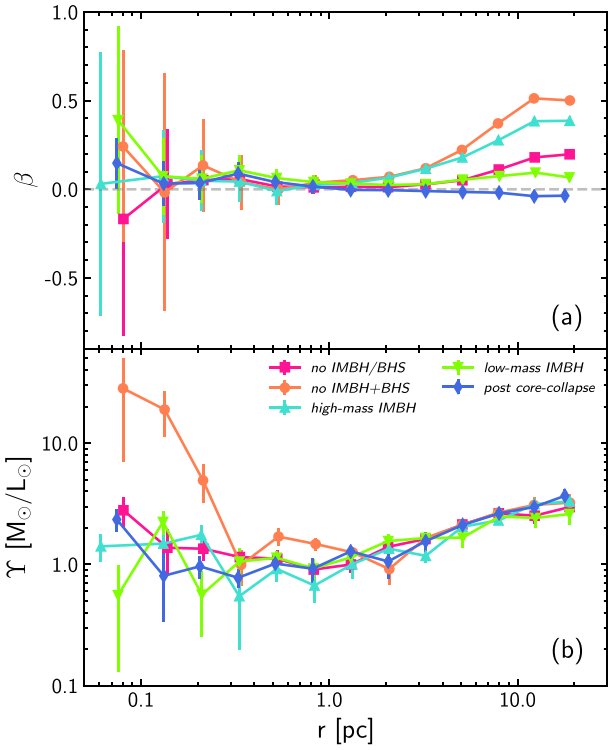

Figure 10. Velocity anisotropy (a) and mass-to-light ratio (b) profiles for each simulation. All simulated clusters, with the exception of the *post core-collapse*, have central velocity anisotropies consistent with being isotropic ($\beta = 0$) and become more radially anisotropic at large radii. The *post core-collapse* cluster is fairly isotropic at all radii. The stellar mass-to-light ratio (Υ) in the simulations varies with radius, increasing towards the centre and the outer regions of the cluster. The central slope of Υ varies with each cluster, where the *no IMBH + BHS* shows the most significant increase due the stellar black holes subsystem at its centre. On the other hand, all simulated GCs show the same behaviour at large radii.

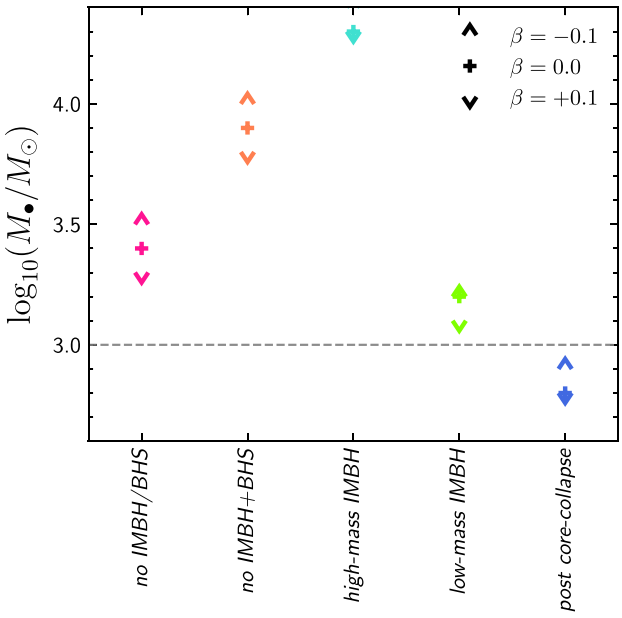

Figure 11. Upper limits of the $\chi^2 \leq 7.8$ region for the central IMBH mass given different velocity anisotropies for the full kinematic data case (LOS + PMs). The tangentially anisotropic case ($\beta = -0.1$, up-red arrow) gives systematically higher upper limits than the isotropic case ($\beta = 0.0$, black crosses) for the inferred mass of the IMBH. On the other hand, the radial anisotropic case ($\beta = +0.1$, down-blue arrow) has systematically lower upper limits, as radial anisotropy can mimic an increase of velocity dispersion in the centre (mass-anisotropy degeneracy).

4 MASS CONSTRAINTS FROM THE JEANS MODELS

The two main assumptions in our dynamical models, which could impact in the determination of the presence of an IMBH and its mass, are firstly the constant mass-to-light ratio and secondly the constant velocity anisotropy (see Section 2.3). As shown in Fig. 10, the internal velocity anisotropy and mass-to-light ratio vary for all five GC simulations. The velocity anisotropy increases at large radii for all GCs, other than the *post core-collapse*. The mass-to-light ratio increases towards the centre and at large radii. While the central mass-to-light ratio depends on the type of central object in the cluster, the rise at large radii is similar for all simulations. In this section, we explore in detail the effects of these factors on our dynamical models.

4.1 Velocity anisotropy

The amount of velocity anisotropy in the central region of the GC can affect the measured mass of the possible central IMBH. A radial velocity anisotropy ($\beta > 0$) at the centre can reproduce an increase of the velocity dispersion without requiring additional mass (i.e. an IMBH). On the other hand, if the central anisotropy becomes more tangential ($\beta < 0$), the model will require an additional mass in the centre of the GCs. This mass-anisotropy degeneracy is well known in dynamical models based on Jeans equations (see Binney & Mamon 1982, for example).

The velocity anisotropy can be constrained by including 3D kinematic data namely proper motions, as discussed in Section 3.2. However, how strongly the anisotropy can be constrained will depend on the quality of the available proper motions. In the case of NGC 5139, van der Marel & Anderson (2010) show that anisotropic models are necessary to describe its observed kinematics and provide good fits to the observed proper motions without the need for a central IMBH, when using models based on Jeans equations. More recently, Zocchi, Gieles & Hénault-Brunet (2017) also show that models based on anisotropic DFs are consistent with the available kinematics of NGC 5139 and while their models do not rule out a central IMBH, they put a cautionary note on the estimated mass of the central IMBH. Both works find a velocity anisotropy profile which is (or close-to) isotropic in the centre. However, while van der Marel & Anderson (2010) find a tangential anisotropy at large radii, Zocchi et al. (2017) find a radially biased anisotropy profile at large radii (before becoming once again isotropic at the tidal radius). The latter is consistent with Watkins et al. (2015), who show that most galactic GCs in the *HST*PROMO sample are isotropic towards the centre and become radially anisotropic at large radii. The upper limit on the possible IMBH mass in NGC 5139 suggests a mass fraction of $M_\bullet/M_{\rm GC} < 0.43$ per cent (van der Marel & Anderson 2010) similar to our *low-mass IMBH* case ($M_\bullet/M_{\rm GC} = 0.30$ per cent). In this regime, the kinematic signature of the IMBH on the observed velocity dispersion profile is not strong enough for a clear detection and it can be reproduced as well by mildly radial anisotropic models ($\beta \sim 0.1$).

Panel (a) of Fig. 10 shows the velocity anisotropy for all five GCs measured directly from the simulations. The low number of stars in the central bins is accounted for with the error bars (through

bootstrapping in each bin). All GCs except for the *post core-collapse* are consistent with being isotropic at their centre and become more radially anisotropic at larger radii, while the *post core-collapse* is consistent with being isotropic at almost all radii. Once we include the proper motions in our dynamical models, the fits become consistent with an isotropic velocity anisotropy ($\beta = 0$, see Figs 8 and 9), while still allowing for models with a more tangential anisotropy (within our error bars). The bias towards tangential anisotropy seems to be a common limitation of standard Jeans modelling approaches (e.g. see Read & Steger 2017).

Fig. 11 shows the effects of anisotropy in the upper limits of the inferred mass of the central IMBH. Models with a fixed tangential anisotropy ($\beta = -0.1$) increase the inferred IMBH mass, while models with radial anisotropy ($\beta = 0.1$) reduce the upper limit. However, given the constraints from the proper motions, the variation on the upper limit of the inferred IMBH mass due anisotropy is not able to exclude the IMBH solution for the cases without one. The upper limits are still above $M_\bullet \sim 1000\,\mathrm{M}_\odot$ ($M_\bullet \leq 630\,\mathrm{M}_\odot$ for the *post core-collapse* GC).

4.2 Mass-to-light ratio

As shown in panel (b) of Fig. 10, the mass-to-light ratio of all simulations is generally not constant. The variation with radius is a direct consequence of the two-body relaxation process of collisional systems such as GCs and it has been systematically observed in simulations (Bianchini et al. 2017; Baumgardt 2017), which in turn has an impact on the mass profiles of our simulated clusters and the constrains from our models.

Fig. 12 shows the cumulative mass profiles [$M(< r)$, left-hand panels] and mass-to-light ratios (Υ, right-hand panels) for all five simulated GCs. The shaded area represents the models with $\Delta\chi^2 \leq 7.8$, while the black line represent the best-fitting model (for the full kinematic sample, i.e. LOS + PMs as in Section 3.2.3); the symbols correspond to the measured values from each simulation. For the *no IMBH/BHS* and *no IMBH + BHS* simulations, the central mass of the GC is poorly constrained. The value of Υ_0 underestimates the central mass-to-light ratio of the cluster as shown in the right-hand panel of Fig. 12. The dynamical model then requires additional mass to generate the observed velocity dispersion towards the centre, allowing for the presence of an IMBH. This effect is evident in the *no IMBH + BHS* case, as the cluster of stellar mass BHs increases drastically the mass-to-light ratio toward its centre. For this case, the inferred mass of the central IMBH is $M_\bullet = 631^{+7312}_{-631}\,\mathrm{M}_\odot$ when using the full kinematic sample. While no false central IMBH is detected, we cannot exclude it either, as the upper limit for such an inferred central IMBH is $M_\bullet < 7943\,\mathrm{M}_\odot$. On the other hand, the presence of a central IMBH will quench mass segregation (see Gill et al. 2008) and in turn change the shape of the mass-to-light ratio profile. This is the case of the *high-mass IMBH* simulation, where the central mass-to-light ratio is well represented by the assumption of a constant mass-to-light ratio (see Fig. 12).

The assumption of constant mass-to-light ratio is not only relevant for the central region of the simulated GCs. As massive particles sink towards the centre, the lighter ones populate the outer regions of the GC. This process also increases the mass-to-light ratio at larger radii, as faint low-mass stars dominate the exterior regions of the cluster. In panel (b) of Fig. 10, we can see that all five simulated GCs have a similar increase in their deprojected mass-to-light ratio profiles at larger radii. In the same way as for the centre of the cluster, our models underestimate the mass-to-light ratios and therefore the mass profiles (see Fig. 12), which in turn could bias the estimates on the cluster

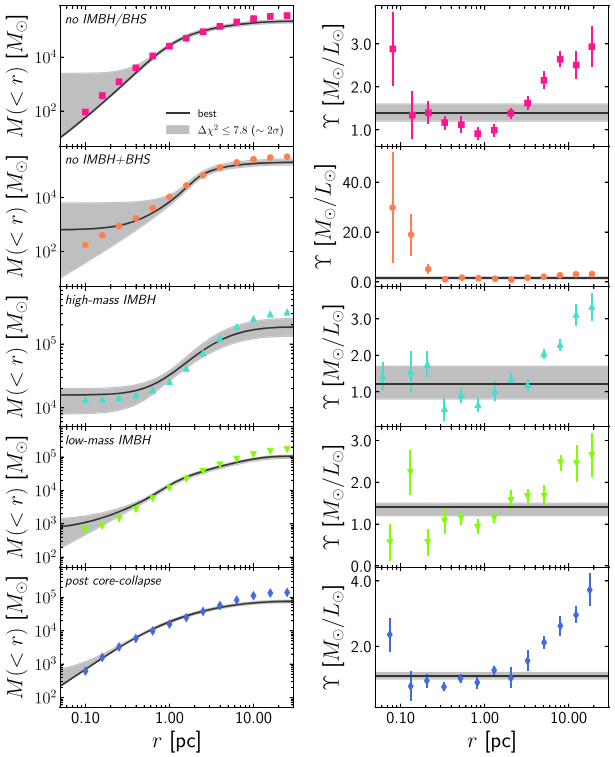

Figure 12. Mass profiles for all the simulated GCs. In the right column, we include the cumulative mass profiles for each simulated GCs as coloured symbols. The black line represents the best-fitting model, when all the velocity data are included in the fit, while the grey shaded area represents the $\Delta\chi^2 \leq 7.8$ region. The models tend to be less constrained towards the centre, in particular, for the *no IMBH/BHS*, *no IMBH + BHS*, and *low-mass IMBH cases*. The right-hand panels show the mass-to-light ratio for each simulation. These profiles differ significantly from the assumption of a constant mass-to-light ratio. The case of the *no IMBH + BHS* simulation is quite extreme as the cluster of stellar-mass IMBH significantly increases the central values of the mass-to-light ratio profile. This is also shown in the cumulative mass profile, where it rises towards the centre instead of declining as in the *no IMBH/BHS* or *post core-collapse* simulations.

mass. Panel (a) of Fig. 13 shows the recovered enclosed mass within the deprojected half-light radius r_h from our dynamical models. For all five simulations, our estimated mass within r_h is consistent with the mass measured directly from the simulation; our fitted values for Υ_0 are in agreement with the expected mass-to-light ratio within $r_{50\text{ per cent}}$ ($\Upsilon_{50\text{ per cent}}$, see Tables 2 and 3, respectively). However, this is not the case at larger radii; panel (b) in Fig. 13 shows that for all simulated GCs, their total masses are within 20 per cent and 40 per cent lower than the expected one. This is in agreement with other works: the effect of mass segregation on the recovering of global properties of GCs was discussed previously by Sollima et al. (2015), where they applied different modelling techniques from multimass DFs to *N*-body simulations of GCs. They show that single mass models systematically underestimate the total mass of the cluster and found that the global parameters are well constrained within the radial range $r_\mathrm{h}/2 < r < r_\mathrm{h}$. In agreement with this, our models have a lower discrepancy on the recovered mass for radii close to r_h (see Fig. A4).

From the discussion above, one can infer that the assumption of a constant mass-to-light ratio has a larger impact on the constrains for the mass profiles, and in turn on the IMBH masses, than the assumption of constant velocity anisotropy. To characterize the

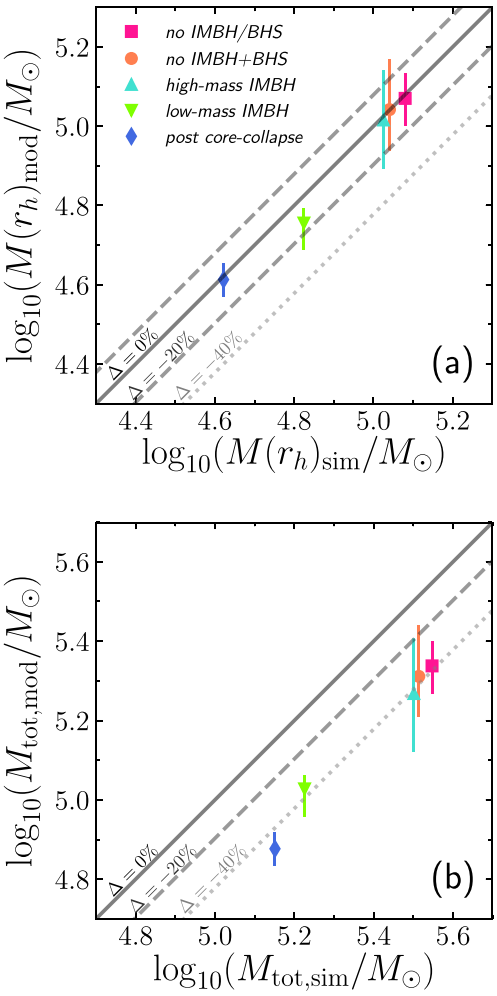

Figure 13. Recovered enclosed mass for the five simulated GCs. Panel (a): the mass within deprojected half-light radius $r_{\rm h}$ is recovered for all GCs (less than 20 per cent error). On the other hand, in panel (b), the total mass of the simulated GCs is systematically underestimated.

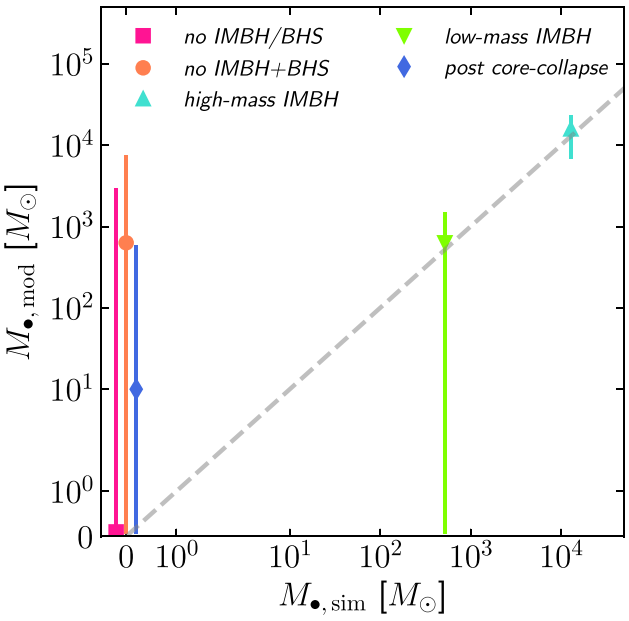

Figure 14. Recovered IMBHs masses from the full 3D kinematic sample (LOS + PMs). Our dynamical models robustly identify the IMBH in the *high-mass IMBH* simulation ($M_\bullet/M_{\rm GC} = 4.1$ per cent). However, lower masses or the absence of the central IMBH cannot be excluded for the *low-mass IMBH* case ($M_\bullet/M_{\rm GC} = 0.3$ per cent). The three simulations without a central IMBH show large upper limits (with an offset from $M_{\bullet,\,\rm sim} = 0.0\,{\rm M}_\odot$ for visibility).

real effect of these assumptions, it is necessary to design a model that includes the variations on the mass-to-light ratio and velocity anisotropy profiles, which is beyond the scope of this paper.

5 SUMMARY

The presence of IMBHs at the centre of galactic GCs is still an ongoing debate. Even with the diverse literature available on the topic (Noyola et al. 2008; van der Marel & Anderson 2010; Lützgendorf et al. 2011; Kamann et al. 2014, 2016; Kızıltan et al. 2017, to name a few), a robust evidence is still missing. Limitations on the observations (such as kinematic centre and crowding, see Noyola et al. 2010; Lanzoni et al. 2013; de Vita et al. 2017) or in the modelling (due to anisotropy or a dark component, see van der Marel & Anderson 2010; Zocchi et al. 2017, 2019; Baumgardt et al. 2019; Mann et al. 2019) make the detection of IMBHs challenging. Here, we explored the limitations of the dynamical model commonly used, namely models based on the Jeans equations. Using five Monte Carlo simulations of GCs with and without central IMBH from the MOCCA survey (see Section 2.2), we have analysed the reliability and limitations of spherically symmetric Jeans models (see Section 2.3) under the assumption of constant mass-to-light ratio and velocity anisotropy. We extracted a kinematic sample from the simulated GCs, excluding all binary systems and selecting stars brighter than 1 magnitude below the main-sequence turn-off (see Section 3.1). We fit the Jeans models to the second velocity moment profiles, varying the mass-to-light ratio (Υ_0), the mass of the central IMBH ($M_\bullet$), and velocity anisotropy (β); we do so for only line-of-sight velocities (LOS, Section 3.2.1), only proper motion velocities (PMs, radial and tangential on the sky, see Section 3.2.2), and the full kinematic sample (i.e. LOS + PMs, in Section 3.2.3).

Our dynamical models can recover the mass of the high-mass IMBH ($M_\bullet/M_{\rm GC} = 4.1$ per cent) quite well (see Section 3.2). The kinematic signature of such an IMBH is strong and the rise in velocity dispersion cannot be explained otherwise. On the other hand for the low-mass IMBH ($M_\bullet/M_{\rm GC} = 0.3$ per cent), we can identify the central IMBH only within 1σ (i.e. $\Delta\chi^2 \leq 3.5$) level, and while the best-fitting model is consistent with the actual mass of the central IMBH ($M_\bullet = 519.3\,{\rm M}_\odot$), models with no IMBH are possible within the errors (note that we consider only kinematic errors due to stochasticity of low numbers of stars per bin; observational errors could increase the uncertainty of the central IMBH mass). For all three simulations without a central IMBH, we get only upper limits and while no IMBH solution is within the range of masses, such upper limits allow for a possible IMBH in their centres. Figure 14 summarizes the recovered IMBH masses for the five simulated GCs.

The dynamical models are limited by two main assumptions: constant velocity anisotropy and constant mass-to-light ratio. Both have different consequences on the upper limits and detection of the central IMBH (see Section 4). Depending on the inferred amount of velocity anisotropy at the centre of the cluster, the dynamical model

can slightly change the required IMBH mass to match the observed kinematics. This is relevant for identifying low-mass IMBHs. The upper limits for the inferred mass of the possible IMBH in NGC 5139 (van der Marel & Anderson 2010) suggest a mass fraction of $M_\bullet/M_{\rm GC} \leq 0.43$ per cent, which is close to our low-mass case ($M_\bullet/M_{\rm GC} = 0.3$ per cent). While both van der Marel & Anderson (2010) and Zocchi et al. (2017) find that anisotropic models are better when compared to the observed velocity dispersion of NGC 5139, the models by van der Marel & Anderson (2010) do not require a central IMBH to explain its observed kinematics. On the other hand, Zocchi et al. (2017) suggest strict upper limits but do not rule out a central IMBH. Better understanding of the velocity anisotropy profiles and the effects of velocity errors on the analysis are necessary to fully disentangle the effects of anisotropy on the inferred mass of low-mass IMBHs. For the cases without an IMBH, we observe that anisotropy alone cannot reduce the upper limits as including the full kinematics sample (LOS + PMs) limits the range of anisotropy that the data allow (see Fig. 11 and Section 4.1).

The assumption of constant mass-to-light ratio has a more significant impact on our analysis, as the mass-to-light ratio increases towards the centre and at larger radii [see panel (b) of Fig. 10]. For the cases without IMBH, we underestimate the central mass due to mass segregation effects (i.e. rise in mass-to-light ratio), which allows the dynamical model to include a central IMBH to recover the observed velocity dispersion. This is even more relevant when the stellar BH retention is higher, such as the case of the model with a stellar BH subsystem (*no IMBH + BHS*). By applying a multimass model that allows for a population of stellar mass BHs at the centre of NGC 5139, Zocchi et al. (2019) show that the population of BHs can reproduce the observed kinematic data, although it cannot discard completely a less massive IMBH. Using a different approach, Baumgardt et al. (2019) also show that the presence of a cluster of stellar mass BHs can explain the observed kinematics of NGC 5139. In their case, they compare the observed kinematics to a library of *N*-body simulations, which intrinsically include a variable mass-to-light ratio.

The assumption of constant mass-to-light ratio limits not only our knowledge of the central mass of the GCs but also its total mass. As two-body relaxation pushes outwards the faint low-mass stars, the mass-to-light ratio increases at large radii. We systematically underestimate the mass-to-light ratio in the cluster outskirts and therefore its total mass, as shown in Fig. 13, is systematically underestimated with a difference of ~ 40 per cent with respect to the expected mass for all simulated clusters. We are able to recover the mass enclosed within the half-light radius, which is consistent with the radial range proposed by Sollima et al. (2015) for estimating global properties of GCs with multimass DFs. Further improvements to our Jeans code are necessary to investigate if we can solve these issues by relaxing the constant mass-to-light ratio assumption.

GCs are collisional systems and their dynamical evolution is tied to the two-body relaxation process. Therefore, it is necessary to include the effects of collisionality in the dynamical models to be able to explain the observed kinematics, even more to robustly identify IMBHs at the centre of GCs. The results of applying our models to the *high-mass IMBH* ($M_\bullet/M_{\rm GC} = 4.1$ per cent) suggest that there is a mass-fraction limit where the effects of collisionality can be excluded from the analysis; finding this limit requires further investigation beyond the scope of this paper. Ultimately, this will help to understand where we must improve the dynamical models. Most GC candidates for having an IMBH are in the low-mass range with $M_\bullet/M_{\rm GC} \lesssim 1.0$ per cent (van der Marel & Anderson 2010), where the kinematic signature can also be explained by the effects of collisionality such as mass segregation, energy equipartition, and a variable mass-to-light ratio. To be able to disentangle the different sources of a velocity dispersion rise in the centre of GC, models that can describe properly the mass profile of GCs are a must. Recently, Hénault-Brunet et al. (2019) provide a compilation of different dynamical methods and their reliability for recovering GC properties. Methods with multiple mass populations and variable mass-to-light ratio significantly improve the recovery of the mass profiles of GCs, although they are still limited by observational constraints and large error bars.

While observational limitations will further complicate the detection of IMBHs in GCs, we have taken the first step in better understanding the ability to recover an IMBH from data with models based on the Jeans equation. The limitations presented here are identical for any such model under the same assumptions, not just ours. While the dynamical models studied here do not lead towards a biased solution, they lack the sensitivity to robustly infer the presence or absence of a low-mass IMBH. Improving a model's ability to recover the mass profiles of GCs, and further understanding how the constant mass-to-light and velocity anisotropy assumptions along with the observed kinematics influence a model, is crucial towards robustly identifying or ruling out the presence of IMBHs in galactic GCs. We will further address observational challenges such as binaries in a subsequent paper.

ACKNOWLEDGEMENTS

We thank the anonymous referee for constructive comments, which greatly improved this manuscript. We thank the MOCCA-Survey collaboration for making their data available to us and answering all our questions. We thank Nadine Neumayer, Laura Watkins, and Manuel Arca Sedda for useful discussions. FIA and GvdV acknowledge funding from the European Research Council (ERC) under the European Union's Horizon 2020 research and innovation programme under grant agreement No 724857 (Consolidator Grant ArcheoDyn). FIA acknowledges funding from DAAD PPP project number 57316058 'Finding and exploiting accreted star clusters in the Milky Way' for a collaboration visit. ACS is supported by the Deutsche Forchungsgemeinschaft (DFG, German Research Foundation) – Project-ID 138713538 – SFB 881 ('The Milky Way System', subproject A08), which also provided PB and AA with funding for a collaboration visit. AMB acknowledges support by the same SFB 881 grant. AA acknowledges support from the Carl Tryggers Foundation for Scientific Research through the grant CTS 17:113 and from the Swedish Research Council through the grant 2017-04217.

This research made use of the NUMPY package (van der Walt, Colbert & Varoquaux 2011), while all figures were made using MATPLOTLIB (Hunter 2007).

DATA AVAILABILITY

The simulated GCs data underlying this article were provided by the MOCCA group[8] by permission. The data will be shared on request to the corresponding author with permission of the MOCCA group. The code to solve the Jeans equations and generate the dynamical models presented in this article will be shared on request to the corresponding author.

[8] https://moccacode.net/

REFERENCES

Abbott R. et al., 2020a, Phys. Rev. Lett., 125, 101102
Abbott R. et al., 2020b, ApJ, 900, L13
Anderson J., van der Marel R. P., 2010, ApJ, 710, 1032
Arca Sedda M., Askar A., Giersz M., 2018, MNRAS, 479, 4652
Arca Sedda M., Askar A., Giersz M., 2019, preprint (arXiv:1905.00902)
Askar A., Szkudlarek M., Gondek-Rosińska D., Giersz M., Bulik T., 2017, MNRAS, 464, L36
Askar A., Giersz M., Pych W., Dalessand ro E., 2018a, MNRAS, 475, 4170
Askar A., Arca Sedda M., Giersz M., 2018b, MNRAS, 478, 1844
Bahramian A. et al., 2017, MNRAS, 467, 2199
Baumgardt H., 2001, MNRAS, 325, 1323
Baumgardt H., 2017, MNRAS, 464, 2174
Baumgardt H. et al., 2019, MNRAS, 488, 5340
Belczynski K., Kalogera V., Bulik T., 2002, ApJ, 572, 407
Belokurov V. et al., 2020, MNRAS, 496, 1922
Bianchini P., Norris M. A., van de Ven G., Schinnerer E., 2015, MNRAS, 453, 365
Bianchini P., van de Ven G., Norris M. A., Schinnerer E., Varri A. L., 2016a, MNRAS, 458, 3644
Bianchini P., Norris M. A., van de Ven G., Schinnerer E., Bellini A., van der Marel R. P., Watkins L. L., Anderson J., 2016b, ApJ, 820, L22
Bianchini P., Sills A., van de Ven G., Sippel A. C., 2017, MNRAS, 469, 4359
Bianchini P., Ibata R., Famaey B., 2019, ApJL, 887, L12
Binney J., Mamon G. A., 1982, MNRAS, 200, 361
Binney J., Tremaine S., 2008, Galactic Dynamics, 2nd ed. Princeton Univ. Press, Princeton, NJ
Breen P. G., Heggie D. C., 2013a, MNRAS, 432, 2779
Breen P. G., Heggie D. C., 2013b, MNRAS, 436, 584
Brodie J. P., Strader J., 2006, ARA&A, 44, 193
Carretta E., Gratton R. G., Clementini G., Fusi Pecci F., 2000, ApJ, 533, 215
Chomiuk L., Strader J., Maccarone T. J., Miller-Jones J. C. A., Heinke C., Noyola E., Seth A. C., Ransom S., 2013, ApJ, 777, 69
Dage K. C., Zepf S. E., Bahramian A., Kundu A., Maccarone T. J., Peacock M. B., 2018, ApJ, 862, 108
de Vita R., Trenti M., Bianchini P., Askar A., Giersz M., van de Ven G., 2017, MNRAS, 467, 4057
de Vita R., Trenti M., MacLeod M., 2018, MNRAS, 475, 1574
Farrell S. A., Webb N. A., Barret D., Godet O., Rodrigues J. M., 2009, Nature, 460, 73
Foreman-Mackey D., Hogg D. W., Lang D., Goodman J., 2013, PASP, 125, 306
Fregeau J. M., Cheung P., Portegies Zwart S. F., Rasio F. A., 2004, MNRAS, 352, 1
Fukushige T., Heggie D. C., 2000, MNRAS, 318, 753
Gebhardt K., Rich R. M., Ho L. C., 2002, ApJ, 578, L41
Giersz M., 1998, MNRAS, 298, 1239
Giersz M., 2001, MNRAS, 324, 218
Giersz M., Heggie D. C., Hurley J. R., 2008, MNRAS, 388, 429
Giersz M., Heggie D. C., Hurley J. R., Hypki A., 2013, MNRAS, 431, 2184
Giersz M., Leigh N., Hypki A., Lützgendorf N., Askar A., 2015, MNRAS, 454, 3150
Giesers B. et al., 2018, MNRAS, 475, L15
Giesers B. et al., 2019, A&A, 632, A3
Gill M., Trenti M., Miller M. C., van der Marel R., Hamilton D., Stiavelli M., 2008, ApJ, 686, 303
Haiman Z., 2013, The Formation of the First Massive Black Holes. Springer, Berlin, Heidelberg, p. 293
Harris W. E., 1996, AJ, 112, 1487
Harris W. E., van den Bergh S., 1981, AJ, 86, 1627
Heggie D. C., Giersz M., 2014, MNRAS, 439, 2459
Hénault-Brunet V., Gieles M., Sollima A., Watkins L. L., Zocchi A., Claydon I., Pancino E., Baumgardt H., 2019, MNRAS, 483, 1400
Hénault-Brunet V., Gieles M., Strader J., Peuten M., Balbinot E., Douglas K. E. K., 2020, MNRAS, 491, 113
Hénon M., 1971a, Ap&SS, 13, 284
Hénon M. H., 1971b, Ap&SS, 14, 151
Heyl J., Caiazzo I., Richer H., Anderson J., Kalirai J., Parada J., 2017, ApJ, 850, 186
Hobbs G., Lorimer D. R., Lyne A. G., Kramer M., 2005, MNRAS, 360, 974
Hunter J. D., 2007, Comput. Sci. Eng., 9, 90
Hurley J. R., Pols O. R., Tout C. A., 2000, MNRAS, 315, 543
Hurley J. R., Tout C. A., Pols O. R., 2002, MNRAS, 329, 897
Hypki A., Giersz M., 2013, MNRAS, 429, 1221
Jeans J. H., 1922, MNRAS, 82, 122
Kamann S., Wisotzki L., Roth M. M., Gerssen J., Husser T. O., Sandin C., Weilbacher P., 2014, A&A, 566, A58
Kamann S. et al., 2016, A&A, 588, A149
Kamann S. et al., 2018, MNRAS, 473, 5591
King I. R., 1966, AJ, 71, 64
Kızıltan B., Baumgardt H., Loeb A., 2017, Nature, 542, 203
Kremer K., Chatterjee S., Ye C. S., Rodriguez C. L., Rasio F. A., 2019, ApJ, 871, 38
Kulkarni S. R., Hut P., McMillan S., 1993, Nature, 364, 421
Lanzoni B. et al., 2013, ApJ, 769, 107
Leigh N. W. C., Lützgendorf N., Geller A. M., Maccarone T. J., Heinke C., Sesana A., 2014, MNRAS, 444, 29
Libralato M. et al., 2018, ApJ, 861, 99
Lützgendorf N., Kissler-Patig M., Noyola E., Jalali B., de Zeeuw P. T., Gebhardt K., Baumgardt H., 2011, A&A, 533, A36
Lützgendorf N., Kissler-Patig M., Gebhardt K., Baumgardt H., Noyola E., Jalali B., de Zeeuw P. T., Neumayer N., 2012, A&A, 542, A129
Lützgendorf N. et al., 2013, A&A, 552, A49
Lützgendorf N., Gebhardt K., Baumgardt H., Noyola E., Neumayer N., Kissler-Patig M., de Zeeuw T., 2015, A&A, 581, A1
Maccarone T. J., Kundu A., Zepf S. E., Rhode K. L., 2007, Nature, 445, 183
Madau P., Rees M. J., 2001, ApJ, 551, L27
Madrid J. P., Leigh N. W. C., Hurley J. R., Giersz M., 2017, MNRAS, 470, 1729
Mann C. R. et al., 2019, ApJ, 875, 1
Mashchenko S., Sills A., 2005, ApJ, 619, 243
Miller-Jones J. C. A. et al., 2015, MNRAS, 453, 3918
Milone A. P. et al., 2012, A&A, 540, A16
Morscher M., Umbreit S., Farr W. M., Rasio F. A., 2013, ApJ, 763, L15
Morscher M., Pattabiraman B., Rodriguez C., Rasio F. A., Umbreit S., 2015, ApJ, 800, 9
Noyola E., Gebhardt K., Bergmann M., 2008, ApJ, 676, 1008
Noyola E., Gebhardt K., Kissler-Patig M., Lützgendorf N., Jalali B., de Zeeuw P. T., Baumgardt H., 2010, ApJ, 719, L60
Portegies Zwart S. F., Baumgardt H., Hut P., Makino J., McMillan S. L. W., 2004, Nature, 428, 724
Read J. I., Steger P., 2017, MNRAS, 471, 4541
Shishkovsky L. et al., 2018, ApJ, 855, 55
Sigurdsson S., Hernquist L., 1993, Nature, 364, 423
Sippel A. C., Hurley J. R., 2013, MNRAS, 430, L30
Sollima A., Baumgardt H., Zocchi A., Balbinot E., Gieles M., Hénault-Brunet V., Varri A. L., 2015, MNRAS, 451, 2185
Spera M., Mapelli M., 2017, MNRAS, 470, 4739
Spitzer L., 1987, Dynamical evolution of globular clusters. Princeton Univ. Press, Princeton, NJ
Spitzer L., Lyman J., 1969, ApJ, 158, L139
Stodolkiewicz J. S., 1982, AcA, 32, 63
Stodolkiewicz J. S., 1986, AcA, 36, 19
Strader J., Chomiuk L., Maccarone T. J., Miller-Jones J. C. A., Seth A. C., 2012, Nature, 490, 71
Tremou E. et al., 2018, ApJ, 862, 16
Trenti M., van der Marel R., 2013, MNRAS, 435, 3272
van der Marel R. P., Anderson J., 2010, ApJ, 710, 1063
van der Walt S., Colbert S. C., Varoquaux G., 2011, Comput. Sci. Eng., 13, 22
Vandenberg D. A., Bolte M., Stetson P. B., 1996, ARA&A, 34, 461

Wang L. et al., 2016, MNRAS, 458, 1450
Watkins L. L., van der Marel R. P., Bellini A., Anderson J., 2015, ApJ, 812, 149
Weatherford N. C., Chatterjee S., Rodriguez C. L., Rasio F. A., 2018, ApJ, 864, 13
Weatherford N. C., Chatterjee S., Kremer K., Rasio F. A., 2019, ApJ, 898, 162
Zocchi A., Gieles M., Hénault-Brunet V., 2017, MNRAS, 468, 4429
Zocchi A., Gieles M., Hénault-Brunet V., 2019, MNRAS, 482, 4713

APPENDIX A: ADDITIONAL FIGURES

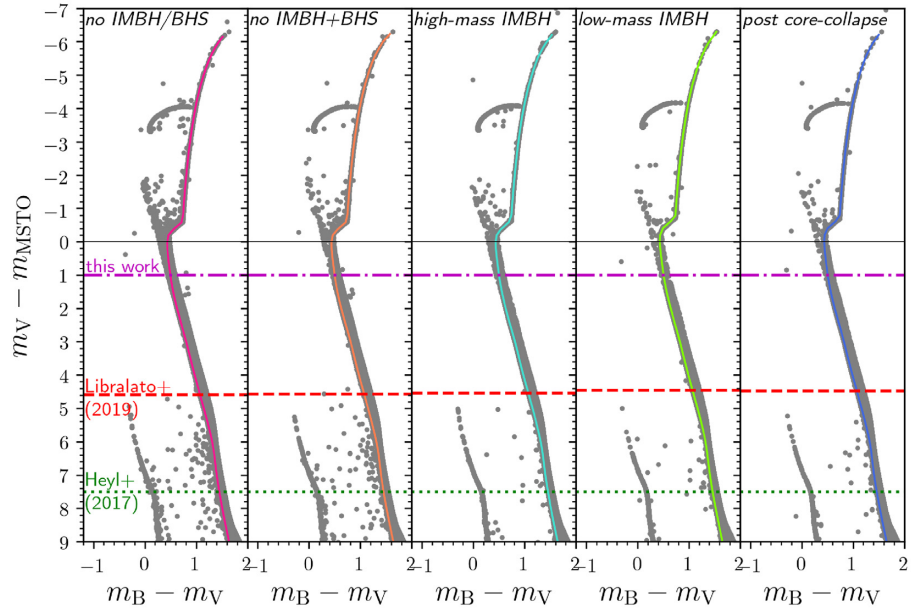

Figure A1. CMD for all five GC simulations, each of them centred at their respective MSTO magnitude. Our selection on magnitude is represented by the dot–dashed line and it is equivalent to select all stars brighter than $m_V \sim 18.5$ at a distance of 5 kpc (as described in Section 3.1) and follows the magnitude limit in Watkins et al. (2015) for *HST* proper motions. For comparison, we include limits from *HST* data for the central (Libralato et al. 2018, for NGC 362) and outer (Heyl et al. 2017, for NGC 104) regions of a GC.

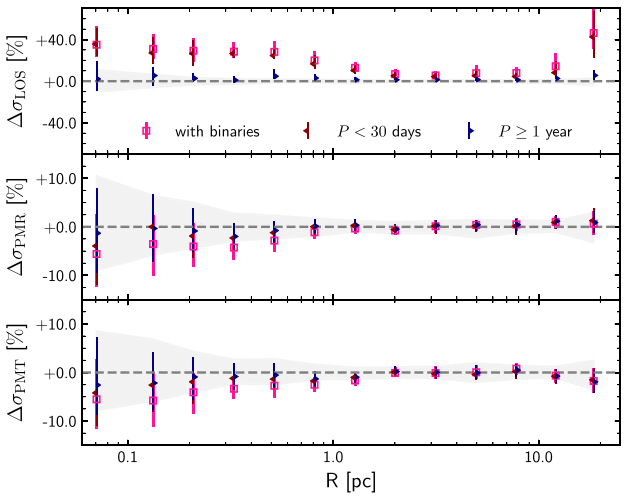

Figure A2. Difference in velocity dispersion for different binary populations relative to the sample without binaries for the *no IMBH/BHS* simulation (as in Fig. 4). Binary systems have different effects in the velocity dispersion for each type of kinematic data. The observed line-of-sight (LOS) velocity of binary systems is mostly dominated by their internal orbital velocity, which translate in an increase in the measured velocity dispersion and it is mostly dominated by short-period binaries ($P < 30$ d). On the other hand, proper motions [radial (PMR) and tangential (PMT) components] are not affected by the internal orbital motion of each component, rather the measured velocity dispersion will be affected by the level of energy equipartition of the binary systems.

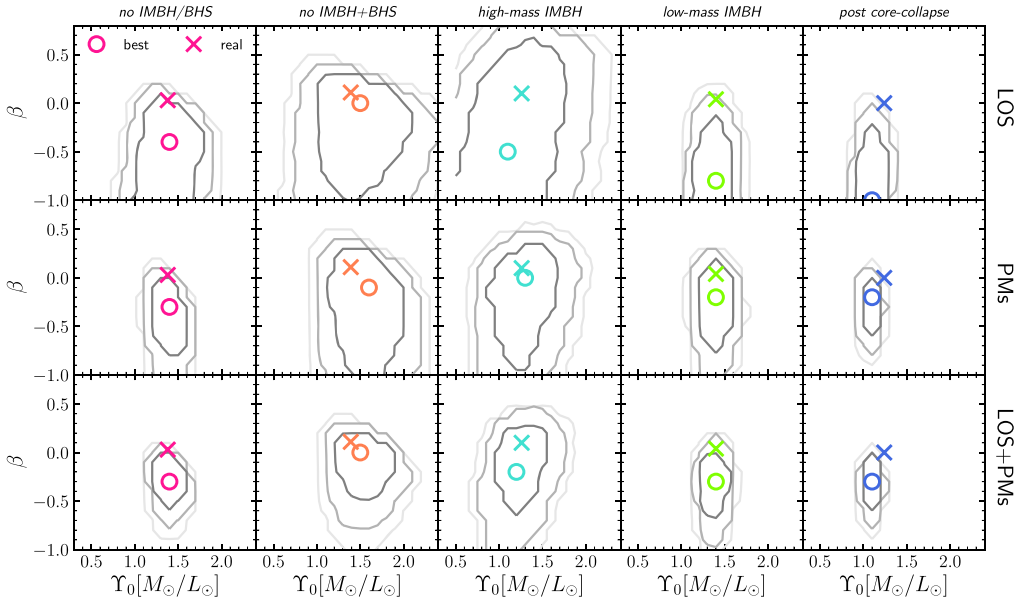

Figure A3. Parameter space for the mass-to-light ratio and velocity anisotropy for all simulations and kinematic data used for the fit. The contours represent the confidence regions we defined to trace the errors, while the open circle represents the best-fitting value in each case, and the x represents the value measured directly from the simulations within the half-mass radius. For most of the simulations, the constraints improve while including more kinematic data. This is not the case for the high-mass IMBH model, where the constraints in the velocity anisotropy do not improve when including proper motions. The central shape of second velocity moment is significantly dominated by the IMBH and the changes due different velocity anisotropy values are watered down by the presence of the high-mass IMBH.

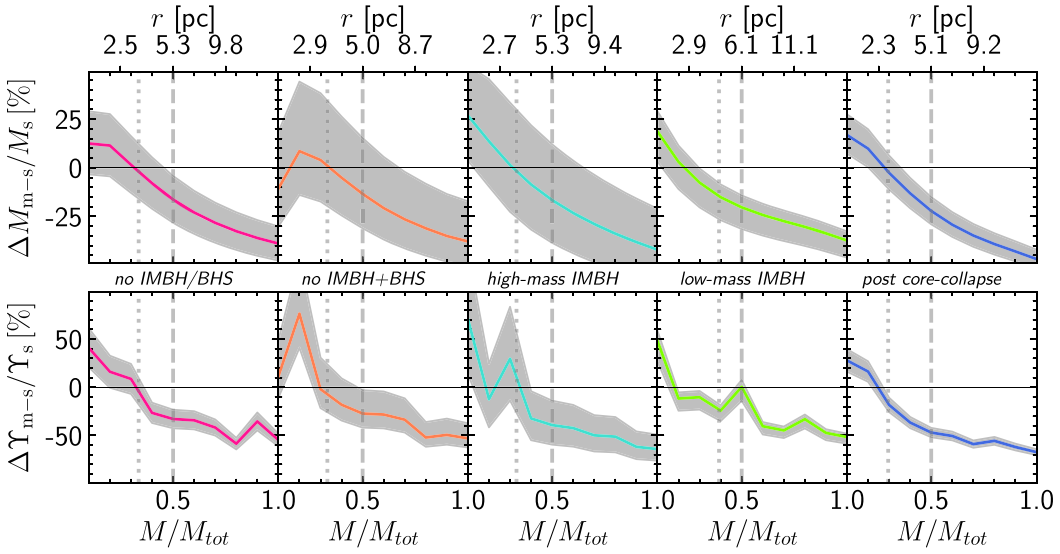

Figure A4. Mass and mass-to-light error per radius for all simulated GCs. For all plots, the x-axis is in mass fraction of the cluster from the centre (Lagrangian radii). The half-mass radius is marked as a vertical dashed line, the deprojected half-light radius is marked as a dotted line. The grey area represents the range of models with $\Delta\chi^2 \leq 7.8$ and the coloured line represents the best-fitting model. On top, we illustrate the values in parsec for three Lagrangian radii as reference. In the top panels, we see that for all five simulated GCs, we systematically underestimate the total mass, while overestimating the inner regions (as we represented the profiles in mass fraction, we are unable to observe the innermost region where the IMBH is relevant). The mass profile errors behaviour by radius is tightly correlated to the difference between our assumed constant mass-to-light ratio and the one from the simulation (bottom panels). In all simulated GCs, the models and the simulations are in agreement (low relative error) around the half-light radius.

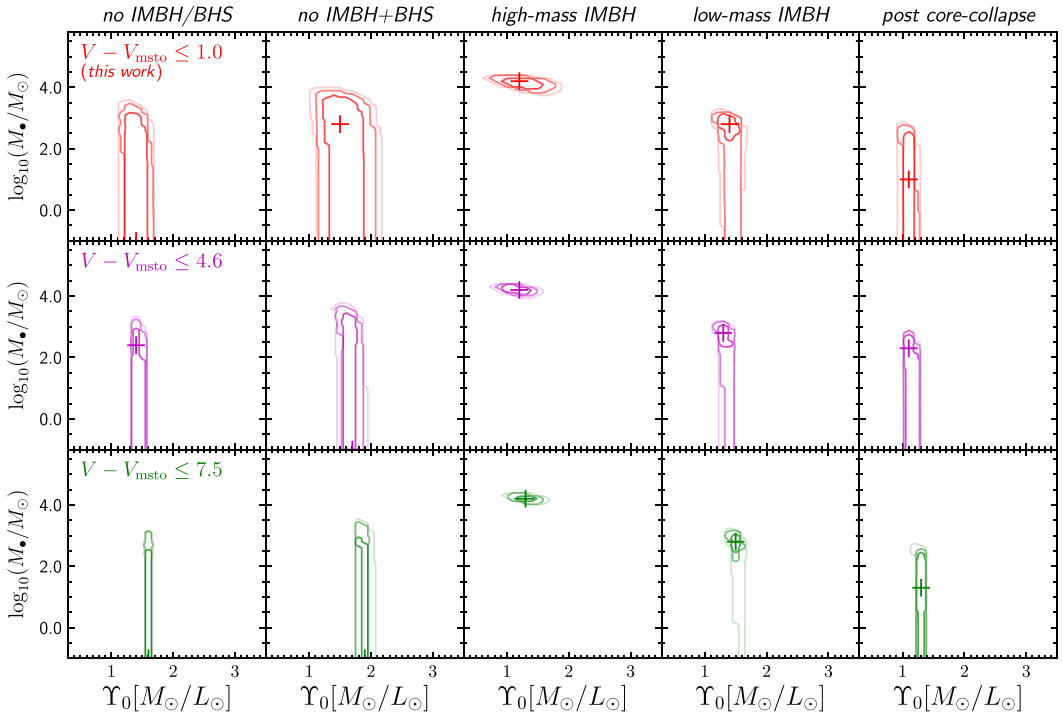

Figure A5. Constraints on the mass-to-light ratio and mass of the possible central IMBH for all simulated GCs (each column), considering the full kinematic sample (as in Fig. 9). Each row indicates a different selection sample in magnitude following the limits in Fig. A1. The constraints are consistent for all cases. Although the second and third rows are beyond the current limits for line-of-sight velocities, while the third is only possible outside $R_{\rm h}$, this comparison shows that the limitations in the modelling described in this work are intrinsic to the model and do not depend on the selected sample. For the *high-mass IMBH* and *low-mass IMBH*, the best-fitting values are consistent with the expected values. On the other hand, for the three GCs without a central IMBH, the best-fitting values of the possible central IMBH do not converge. Once deeper observations are available allowing for a fainter limit in the luminosity cut, the Jeans modelling will automatically produce better results as our stochastic errors decrease with more stars in each bin.

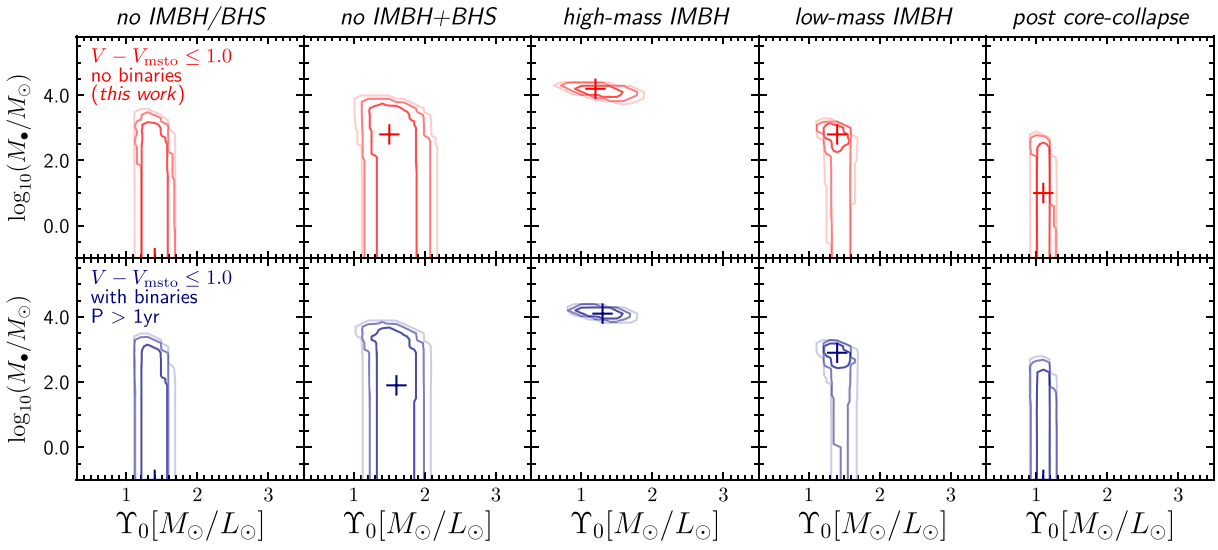

Figure A6. As in Fig. A5, but considering different binary samples. The first row corresponds to the case without binaries as in our main analysis, while the bottom row shows the case when long-period binaries ($P > 1$ yr) remain in the kinematic sample. The constraints from both cases are similar. As shown in panel (b) of Fig. 4, the sample with contamination from long-period binaries is consistent with the case without binaries (within errors), which is reflected on the parameter space.

This paper has been typeset from a TEX/LATEX file prepared by the author.